Synthesis, characterizations and performance evaluation of $Ag/Ag_2O/ZnFe_2O_4$ composite materials for organic dye degradation

By

Sorome Diriba Temesgen

M.Sc. thesis submitted to the Department of Materials Science and Engineering

School of Mechanical, Chemical and Materials Engineering

Presented in partial fulfillment of the requirement of M.Sc. Degree in Materials Science and Engineering

Office of postgraduate studies

Adama Science and Technology University

Adama, Ethiopia

July 2020

Synthesis, characterizations and performance evaluation of $Ag/Ag_2O/ZnFe_2O_4$ composite materials for organic dye degradation

Sorome Diriba Temesgen

Advisor: Dr.Temesgen Debelo (Ph.D.)

Co-advisor: Dr. Gebisa Bekele (Ph.D.)

Materials Science and Engineering Department

School of Mechanical, Chemical and Material Engineering

Presented in partial fulfillment of the requirement of M.Sc. Degree in Materials Science and Engineering

Office of postgraduate studies

Adama Science and Technology University

Adama, Ethiopia

July, 2020

Advisor Approval sheet

To: Materials Science and Engineering Department

Subject: Thesis Submission

This is to certify that, the thesis entitled "Synthesis, characterizations, and performance evaluation of $Ag/Ag_2O/ZnFe_2O_4$ composite materials for organic dye degradation". This thesis was submitted in partial fulfillment of the requirement for the degree of Masters in Material Science and Engineering postgraduate program of the department of Materials Science and Engineering and has been carried out by Sorome Diriba Temesgen; Id.NoPgr/18161/11, under our supervision. Therefore, we recommended that the student has fulfilled the requirements and hence she can submit the thesis to the department.

Advisor	Signature	Date
Co-advisor	Signature	Date

Declaration

Here by, I declared this thesis work is my original work not done by other researchers for the fulfillment of any degree in any university yet. In addition, the materials used in this thesis work have been acknowledged.

_____	_____	_____
Student	Signature	Date
_____	_____	_____
Advisor	Signature	Date
_____	_____	_____
Co-advisor	Signature	Date

Approval of Board of Examiners

We the final defense examiner board for the thesis entitled with "Synthesis, characterizations, and performance evaluation of $Ag/Ag_2O/ZnFe_2O_4$ composite materials for organic dye degradation" presented by Sorome Diriba Temesgen examined and approved the thesis. Therefore, this is certifying that the thesis has been accepted in a partial fulfillment of the degree of Masters in Materials Science and Engineering.

Advisor	Signature	Date
Chairperson	Signature	Date
Internal Examiner	Signature	Date
External Examiner	Signature	Date

ACKNOWLEDGEMENT

First, I would like to thank almighty GOD for his everlasting mercy and support. Then after, I would like express my deep gratitude and respect to Dr.Temesgen Debelo Desissa, Dr. Osman Ahmed Zelekew, Dr. Dinsefa Mensur Andoshe and Dr Gebisa Bekele for their guidance, constructive criticism and valuable suggestion.

My deep gratitude goes for my families for their support and encouragement. In addition, my special thanks goes for Mr. Demeke Tesfaye, for his patience, inspiring support and facilitation, throughout all of the libratory activities of this research work. I would also like to extend my deep gratitude to all of my colleagues and Material Science and Engineering staff members for their constructive advice and encouragement supports throughout this research work.

Lastly, I would like to thank Materials Science and Engineering Department and Adama Science and Technology University for providing this Masters scholarship and funding this research work under the grant number ASTU/SM-R/130/19.

Abstract

Processing industries such as leather, textile, paper, food and cosmetics uses various chemicals during their operations and therefore, produce large amount of industrial effluents containing environmentally toxic substances such as organic dyes and other heavy metals. Most of the organic dyes are biologically non-degradable if released to the environment and pose a threat to human health. Thus, these toxic substances can be converted to non-toxic substances using photo-catalyst materials through degradation process. In this work, (x)Ag_2O/(1-x) $ZnFe_2O_4$ (with x= 0.05, 0.1, 0.15 and 0.2) composite materials were prepared by decorating Ag_2O on previously green method synthesized $ZnFe_2O_4$. The green synthesis was achieved by using Ajuga integrafolia plant as a capping/stabilizing agent. Optimization of the binary composites was investigated with respect to performance and the composite with a composition of x = 0.15 or 15 % of Ag_2O denoted by AZW-3 showed an optimum value. The effect of calcination temperature on the optimum binary composite and formation of Ag were studied in a temperature range of 260–300 °C, with an optimum calcination temperature at 280 °C. Moreover, the effect of the Ag_2O content (weight %) in (x)Ag_2O/(1-x) $ZnFe_2O_4$ (with x = 0.05, 0.1, 0.15 and 0.2) subjected to calcination temperature of 280°C on performance was investigated.

Thermal analysis, phase purity &chemical composition, microstructure, and elemental analysis was performed, respectively, using thermogravimetric–differential thermal analyzer (TGA - DTA), X-ray powder diffraction (XRD), Fourier-Transform infrared (FTIR), and Scanning electron microscopy/Energy Dispersive Spectroscopy (SEM/EDS).

*Moreover, the photocatalytic performance of the synthesized materials was evaluated through degradation of an organic dye – methylene blue (MB) –under visible light source irradiation. The performance was evaluated by varying pH of the MB for the composite with optimized performance. Ultraviolet (UV)-visible spectroscopy was used to analyze the concentration of the MB before and after degradation performance at a time **t**, and thus the corresponding reaction kinetics. The composite with a composition of 15wt% of Ag_2O in (x)Ag_2O/(1-x)$ZnFe_2O_4$ denoted by AAZW-3 subjected to a calcination temperature of 280 °C showed an optimum degradation performance around 90% within 80 min. Moreover, the optimum sample showed best performance in basic media (at a pH around 10). This study suggests that the present materials systems have a potential of degrading an organic dye from the industrial effluents discharged from the various processing industries.*

Table of Contents

List of tables

List of figures

List of acronym

AOPs - Advanced Oxidation Process

BET- Bruneur Emmit Teller

CB- Conduction Band

DTA- Differential Thermal Analysis

E - Energy

EDS- Energy Dispersive Spectroscopy

FTIR - Fourier Transformation Infrared Spectroscopy

FWHM - Full Width at Half Maximum

FTIR - Fourier Transformation Infrared Spectroscopy

MB - Methylene blue

NHE - Normal Hydrogen Energy

PL - Photo Luminescence

SEM - Scanning Electron Microscope

SSA- Specific Surface Area

TEM - Transmission Electron Microscope

TGA -Thermo Gravimetric Analysis

XRD - X-ray Powder Diffraction

CHAPTER ONE

1. Introduction

1.1. Backgrounds

Recently environmental pollution such as contaminations of water bodies by industrial wastewater becomes the major concern and priority for the environment. Based on their toxicity type, water body pollutants can be classified broadly into chemical, pathogenic and radioactive pollutant [1, 2]. Chemical pollutants (contaminants), among other types, could cause an enormous effect on the human health due to their release in trace amounts from the industries to the environment [3]. Organic and inorganic pollutants are sub-classes of the chemical contaminant, where the former contaminant is one of the hazardous and non-biodegradable due to its physicochemical properties [1, 2]. Organic dyes are typical examples of organic contaminants, which are discharged with trace amount from leather, paper, food, cosmetics industries to the environment, causing several health related issues such as skin irritation, cancer, pregnancy problems, birth defects, and so on [4]. Moreover, these contaminants could cause challenges that could lead to ecological problems through consumption of the oxygen molecules in the water bodies [5]. Therefore, these contaminants have to be removed and/or converted to non-toxic molecules as efficiently as possible before their discharge to the environment.

Several techniques have been developed for the removal and conversion of these contaminants. Some of them include flocculation, adsorption, coagulation, biodegradation, sedimentation, membrane process and soon [6-9]. However, these techniques are insufficient due to the complex composition and different physico-chemical properties of the contaminants as well as the low efficiency, high-energy consumption and risk of secondary pollutant formation of the techniques [7, 9-11]. Moreover, the organic pollutants are non-degradable by traditional techniques due to the presence of stable aromatic groups in the structure of organic pollutants [1]. Therefore, an alternative technique with high efficiency, low energy consumption and environmentally friendly is desirable for the treatment of the industrial effluents to remove and convert them to non-toxic molecules and substances. One of the alternative approaches to treat the industrial effluent is photocatalysis, which uses photon energy and oxide semiconductor nanomaterials as a catalyst to degrade organic contaminants. Some of these oxide nanomaterials include titanium dioxide (TiO_2)

[12, 13], Zinc oxide (ZnO) [14-17], spinel structured ferrite materials (AB_2O_4, A= Zn, Co, Cu, B=Fe) [18-20], and other oxide nanoparticles used for degradation of the organic dye from the industrial effluents. Among the various ferrite materials, $ZnFe_2O_4$ is widely used for the photocatalytic application due to high magnetic separation properties, photochemical stability, non-toxicity and narrow band gap (E_g = 1.9 eV) [21]. However, the photocatalytic performance of $ZnFe_2O_4$ is limited by the rapid charge recombination [22], which leads to the decrease in degradation efficiency. To minimize the charge carrier recombination of $ZnFe_2O_4$, researchers combined a *p*-type semiconductors such as BiOCl [23], AgI [24], Ag_2O [22, 25], $BiMoO_6$ [26] with n-type ZnFe2O4 as a result a hetero-junction is formed. The formation of p-n junction leads to the elongation of charge carrier recombination time due to the formation of depletion region between the p-type and n-type semiconductor junction [24]. Moreover, the plasmonic effect through the incorporation of Ag metal in the $ZnFe_2O_4$ based hetero-junction semiconductors [2, 24, 27-29] can further reduce the charge carrier recombination processes and thereby increases the photocatalytic performance of the hetero-structure.

In this work, a plant type *Ajuga intergrafolia (remota)* was used as a capping/stabilizing agent for the synthesis of $ZnFe_2O_4$ using green synthesis method. Facile deposition-precipitation method was used to synthesize composite of $Ag_2O/ZnFe_2O_4$. Using facile precipitation, followed by calcinations, Ag_2O in the $Ag_2O/ZnFe_2O_4$ was partially decomposed to Ag so that plasmonic effect can be introduced to the structure. Characterizations such as thermal analysis using TGA-DTA, phase purity investigation using XRD, chemical composition analysis using FTIR, and microstructure and morphology study by using SEM/EDS were performed. Then, the photocatalytic performances of the synthesized samples were investigated.

1.2. Statement of the problem

Nowadays, a requirement of efficient and recoverable photocatalyst for organic dye removal from industrial wastewater is a challenging issue. $ZnFe_2O_4$ is promising material due to its recoverability and visible light absorption. However, photocatalytic performance of $ZnFe_2O_4$ is limited by the rapid charge recombination because of its lower band gap energy (1.9 eV/NHE). To inhibit the charge carrier recombination of $ZnFe_2O_4$, many research works have been done. Among them is coupling of Ag_2O with $ZnFe_2O_4$, which effectively enhance the photocatalytic performance of $ZnFe_2O_4$ due to longer recombination time. However, further work is required to accelerate charge separation, increasing charge density and specific surface area of the photo-

catalyst without hindering the magnetic separation of $ZnFe_2O_4$. Green synthesis approach of $ZnFe_2O_4$ using *Ajuga integrafolia* plant as capping/stabilizing agent to increase specific surface area can be used. Moreover, in the process of $Ag/Ag_2O/ZnFe_2O_4$ fabrication, Ag ion, which is generated due to the partial decomposition of Ag_2O, plays a plasmonic effect that suppresses charge carrier recombination and generates electrons on its surface.

1.3. Objectives

1.3.1. General objective

To synthesis, characterize and evaluate the photocatalytic performance of $Ag_2O/ZnFe_2O_4$ by introducing Ag through reduction of Ag_2O by calcinations for enhanced organic dye degradation.

1.3.2. Specific objectives

- Extraction of *Ajuga integrafolia* plant leave and synthesis of $ZnFe_2O_4$ using the extract solution
- Synthesis of $Ag_2O/ZnFe_2O_4$ composite using facile deposition-precipitation method
- Reduction of Ag_2O in the $Ag_2O/ZnFe_2O_4$ composite to introduce Ag into $Ag_2O/ZnFe_2O_4$ for plasmonic effect through calcinations of the composites
- Characterizations of the synthesized samples
- Evaluate the photocatalytic degradation efficiency of methylene blue (MB) by the synthesized photocatalytic materials

1.4. The scope of the research

In this work, extraction of *Ajuga integrafolia* plant and synthesis of $ZnFe_2O_4$ by using plant extract as a stabilizing/capping agent was performed. Moreover, $Ag_2O/ZnFe_2O_4$ composite was synthesized by using facile deposition-precipitation method. Furthermore, partial-decomposition of Ag_2O in the $(x)Ag_2O/(1-x)\ ZnFe_2O_4$ (with x = 0.05, 0.1, 0.15 and 0.2) was carried out to introduce the Ag into $Ag_2O/ZnFe_2O_4$. The synthesized sample was characterized by different techniques. Finally, the performance evaluation of the synthesized samples were investigated by using methyl blue (MB) dye and the effect of pH on the degradation capacity of the optimum material was investigated by adjusting the pH of the solution to acidic, neutral, and basic, i.e., 3, 7, and 10, respectively.

1.5. Significance of the study

This work primarily benefits the industries such as textile, paper, cosmetic and leather processing which release effluent with high concentration of organic dyes. Furthermore, the environmental pollution by these organic dyes will also be reduced. The deterioration of released organic contaminant minimizes the exposure of human being to this contaminant and decrease the amount of oxygen that could be absorbed by this contaminant. From human health point of view, the problem such as cancer, mutation and skin irritation caused by organic dyes could be also minimized.

CHAPTER TWO

2. Literature review

In this chapter, industrial effluents such as organic contaminant in wastewater and their effects and impacts on the human and the environment is discussed. Moreover, the removal ways of the contaminants from the wastewater and the techniques used for the treatment of the water are listed. Among them, the effective technique is a photo-catalysis, which is discussed briefly in this chapter with its working mechanism (organic dye degradation) and the corresponding factors affecting the degradation process.

The other portion of this chapter covers materials used as a photocatalyst, which can be used for the wastewater treatment with their limitations as well as their advantages.

2.1. Industrial wastewater

Now-a-days, environmental pollution by industrial wastewater becomes the major concern and priority for the world, especially for the industrial nations. Industrial wastes, mining activities, sewage and wastewater, pesticides, and chemicals, fertilizers, energy use, radioactive waste and urban development etc are playing a great role in water pollution as well as environmental pollution at large [30]. In fact, if water is used for the agriculture, domestic or industrial purpose it will become polluted due to the processes utilize different types of chemical and the exposure of the water the microorganism around there. The water pollutants are classified into radioactive, chemical and microbial contaminants [3]. The intake of these contaminants has adverse effect in human health: the pathogenic contaminant frequently lead to gastro interstitial illness and the chemical one may damage the major organs, functional systems and increase the risk of cancer [3]. Among these, the chemical contaminants has a credible effect on the human health and released with trace amount from the industries [3]. The organic contaminant is one of the chemical contaminant types, which are hazardous for human being due to uneasy degradability of the contaminant because of the aromatic groups in the structure of the organic pollutants [1, 2]. Figure 2.1 is an illustration on the category of the various types of contaminants polluting water.

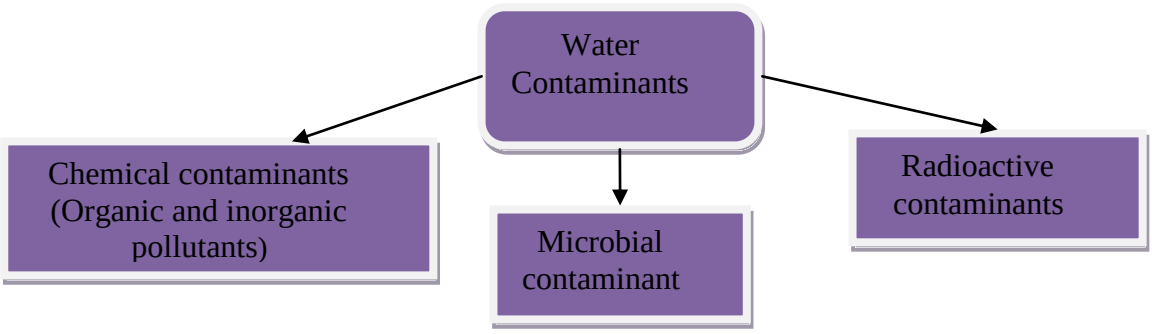

Figure 2.1 Types of water contaminants.

Organic dyes are one of the organic contaminants, which are released from different industries. These type of contaminants can cause mutation, cancer and skin irritation [4]. They also reduce the amount of the oxygen content in the water and leads to ecological problem [5]. Therefore, the industrial wastewater must be treated effectively for the sake of the human and environmental well-being.

2.2. Industrial wastewater treatment techniques

Industrial wastewater treatments are crucial activity for the human and the environmental well-being. To treat the wastewater, several techniques can be used. These techniques can be physical, chemical, and biological techniques, including coagulation, bio-coagulation, electro-coagulation, plasma treatment, filtration, electro-chemical treatment, biodegradation, evaporation, adsorption and ion exchange [6-9]. However, they are insufficient due to the complex composition and different physicochemical composition of the contaminants, as well as the low efficiency, high initial cost, high energy consumption like electricity and risk of secondary pollutants of the techniques which cause human disease such as cancer and Alzheimer's [7, 8]. Therefore, an alternative industrial effluent treatment is required. For the past 30 years, the advanced oxidation processes (AOPs) are used for the degradation of the organic dyes. Among the AOPs, the heterogeneous photocatalysis is widely used due to complete mineralization of the contaminant, no waste disposal, necessity of mild temperature and pressure [31, 32].

2.2.1. Conventional and advanced oxidation process

Coagulation is a process used for industrial wastewater treatment, which utilizes coagulants (organic or inorganic) to hydrolyze, and adsorbed to the surface of the contaminant to produce

simple soluble products [9-11]. The produced sludge from the process causes Alzheimer disease [33]. Filtration is other type of effluent treatment method, which separates the contaminant and the water by using clay, membrane or nanomaterials [9]. But filtration is not effective in organic contaminant removal due to their composition [9]. Ozonation and Fenton reaction can be used for organic dye degradation. However, the Ozanation process needs high electric energy power, which is expensive, and the Fenton one produced a secondary pollution such as iron sludge [34, 35].

2.2.2. Photocatalysis

Photocatalysis is a reaction which accelerated by light energy in the presence of semiconductor material. The induced light generate the electron and holes from the semiconductor for the oxidation and reduction reaction respectively, holes are farther used to produce hydroxide radical, which degrade the pollutant into carbon dioxide and water [5]. This process has advantages than other wastewater treatment techniques due to the complete mineralization of the pollutants, no waste disposal problem, necessity of mild temperature and pressure condition [31, 32].

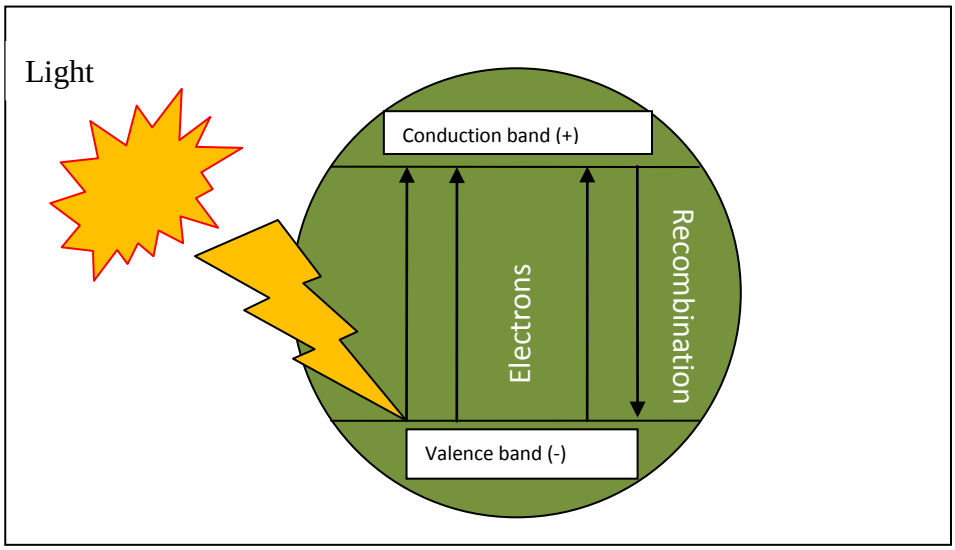

Figure 2.2 Schematic representation of electronic structure of semiconductor.

Semiconductors are preferable for photocatalysis due to their unique electronic properties, the filled valence band and empty conduction band, response to the light energy by moving the electron from the valence band to conduction band which is equal to their band gap energy [36].

2.2.2.1. Photocatalysis mechanism

Light (photon) energy is the primary driver of the photocatalytic reaction. In this reaction, the electrons in the valence band are agitated and move to the conduction band of the semiconductor

(catalyst), when light energy in terms of photon which is equivalent or greater than the band gap of the semiconductor fall on the semiconductor [37]. The electrons and the holes generated in this process used for reduction and oxidation reaction respectively. Additionally electrons in the conduction band react with the dissolved oxygen species to form the superoxide radical and the holes react with the water to produce hydroxyl radicals [38]. Hydroxide radical plays a detrimental role in the degradation of organic pollutants [1, 5, 31, 37, 39-51].

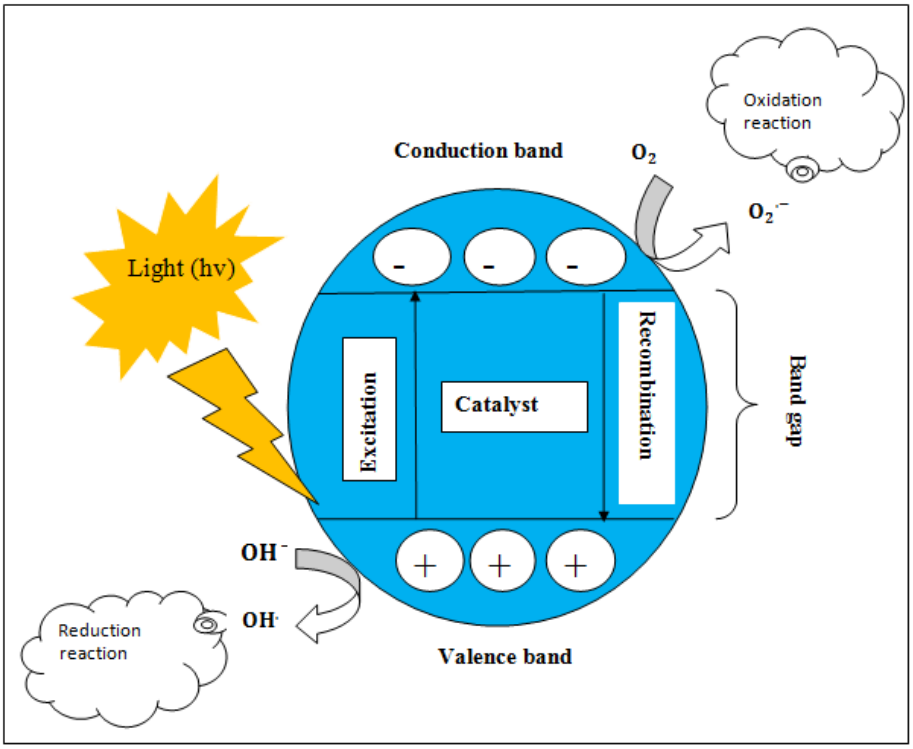

Figure 2.3 Schematic representations of photocatalysis.

2.2.2.1.1. Oxidation reaction

The positive holes created in the valence band of the semiconductor due to the electron shift to the conduction band because of light radiation oxidize the water, which is absorbed to the surface of the semiconductor during the reaction to form hydroxyl radicals in wastewater treatment. Afterward, the formed hydroxide radicals react with the organic matter present in the dyes due to the decomposition power of the hydroxide radicals. If there is oxygen during the process, the intermediate organic molecules and the oxygen experience radical chain reaction by consuming the dispersed oxygen, the organic molecules finally decomposed to carbon dioxide and water. Under such circumstance oxidative decomposition occur as a result of the direct reaction of the positive holes and organic compounds [52, 53].

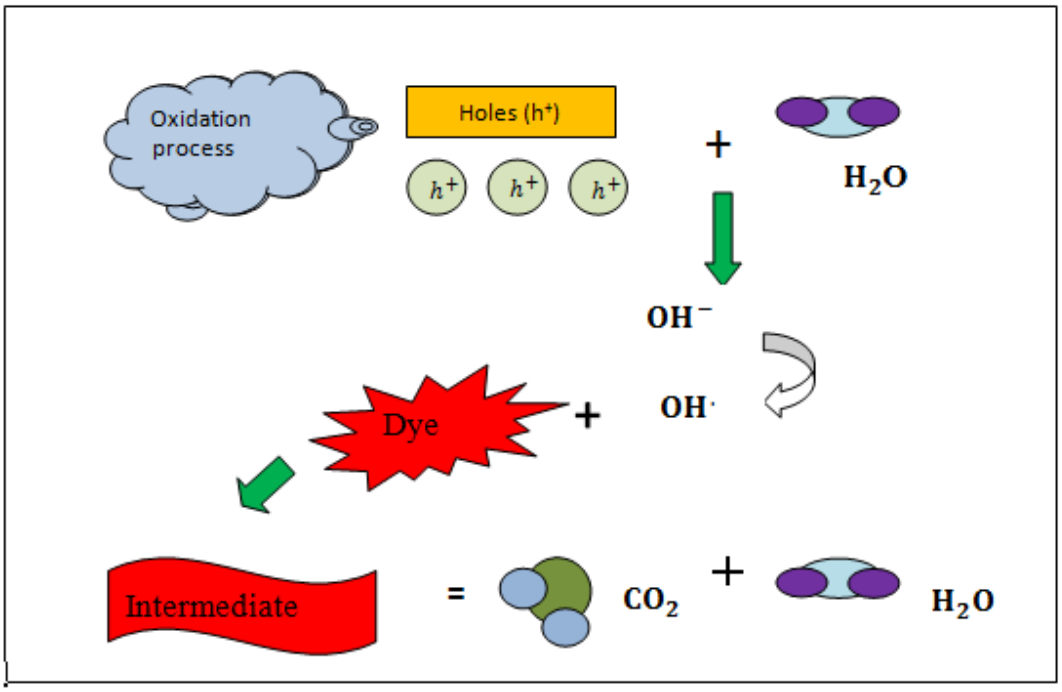

Figure 2.4 Schematic representation of oxidation processes.

2.2.2.1.2. Reduction reaction

In the reduction reaction, the reduction of the oxygen takes place, when the dissolved oxygen reacts with the conduction band electron to form the superoxide. The produced super oxides are attached to the intermediate product produced in the oxidation reaction to yield peroxide or hydrogen peroxide which finally changed to water [52]

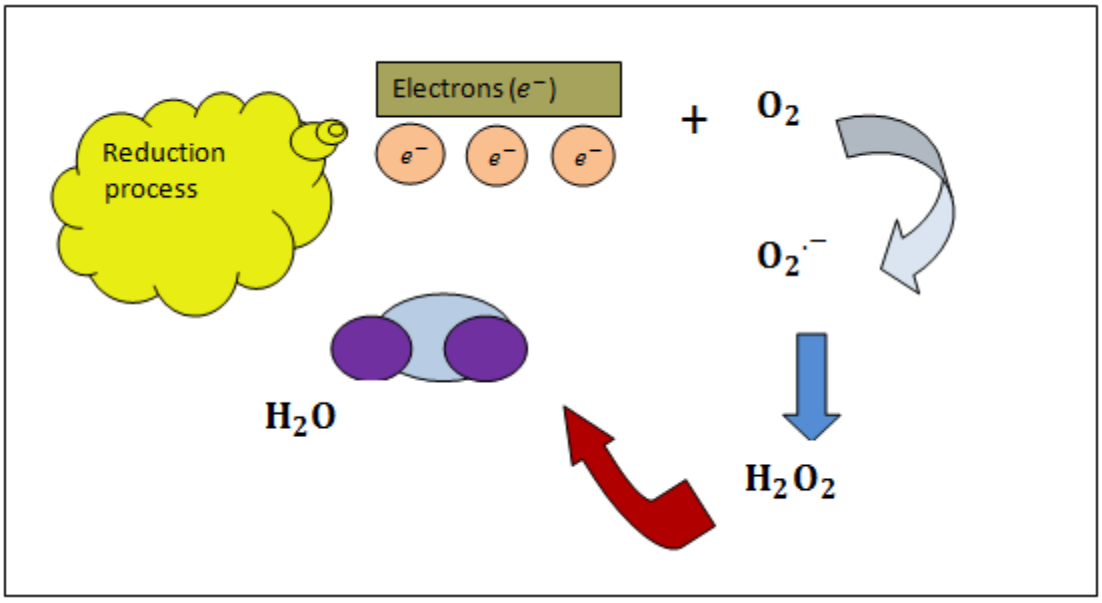

Figure 2.5 Schematic representation of reduction reaction.

2.2.2.2. Factor affecting photocatalysis reaction

Factors such as size, shape and surface area of catalyst, reaction temperature, pH, amount of the catalyst and the concentration of wastewater affect the mineralization process of organic pollutants [54-56].

2.2.2.2.1. Effect of pH

The pH of a solution affects the photocatalytic degradation of the organic pollutants by determining the surface charge properties of the photocatalyst [54, 57, 58]. Shourong *et al* reported that the change in pH affects the efficiency of degradation of organic pollutants [54]. The photocatalytic degradation of $ZnFe_2O_4$@CMC material for CIP degradation was done under different pH. In acidic and basic media both CIP and $ZnFe_2O_4$@CMC are negatively and positively charged respectively which forms a repulsion force between the pollutant and the photocatalyst has a negative effect on the degradation of CIP [54]. The highest photocatalytic removal is shown at neutral pH because of no electrostatic interaction occurs [54]. The effect of the pH on the rate of reaction of the photocatalysis can be determined depending on the electrostatic interaction of the photocatalyst and the pollutant which influence the surface property and adsorption [54].

2.2.2.2.2. Effect of light intensity

The light intensity affects the degradation rate of photocatalytic reaction through initiating the reaction, which is due to the formation of electrons and holes. The absorbed light by the photo catalyst or reactant are equal to quantum yield, which is the ratio of the rate of reaction to the rate of absorption of radiation. The variation of wavelength of light source varies the photocatalytic activity of the photocatalyst. The TiO_2 catalyst absorb in the UV region due to its large band-gap (3.2 eV) [55]. Moreover, the degradation efficiency of the TiO_2 is affected by the absorbed light intensity as the light intensity increase in the range of 0-20 MW/cm^2 the reaction rate increase [55]. The reaction rate decrease at high intensity light radiation, which leads to more electron-hole recombination in the TiO_2 catalyst. There is more electron–hole recombination at excessive light intensity radiation [55].

2.2.2.2.3. Effect of reaction temperature

Temperature is one factor which decrease the photocatalytic activity by enhancing the electron-hole recombination and desorption of adsorbed reactant species when the temperature exceed the optimum temperature [59-61]. Ahmed S *et al*. investigate the effect of reaction temperature by varying the temperature between 20-80 °C for degradation of organic dyes (Methyl blue and Indigo carmine) using CA-CNT/TiO_2-NH_2 [61]. The degradation efficiency of the CA-CNT/TiO_2-NH_2 photocatalyst increases when temperature increases [61]. Yanjun X *et al*. also demonstrate as the photocatalytic reaction temperature affects the degradation efficiency of the photocatalyst by utilizing as synthesized CuS-CdS/TiO_2 nano-boats for the degradation of Toluene at 20, 30, 40 and 50 °C reaction temperature. Initially the photocatalytic efficiency of the photocatalyst increase with the temperature and decrease after 40 °C due to the adsorption desorption equilibrium achieved at a higher temperature is not adequate enough [62].

2.2.2.2.4. Effect of shape, size and surface area of the photocatalyst

The performance of the photocatalyst is affected by the change in the morphology of the catalyst; as the shape changes the surface area also change. Spherical shaped ZnO showed higher photocatalytic performance than spindle and rod shaped ZnO due to its large surface area [63, 64]. In addition to the shape of the photocatalyst, the size also affects the photocatalytic activity. Higher photocatalytic activity is achieved when the size of the catalyst decrease which leads to the enhancement of the active sites and interfacial charge carrier transfer rates [65]. The bulk TiO_2

showed the lowest photocatalytic performance when compared to the nanosized TiO_2 photocatalyst [65]. As it is know the heterogeneous photocatalysis mainly takes place in the surface of the photocatalysts and so then the surface properties significantly influence catalyst performance [66].

2.2.2.2.5. Effect of amount of catalyst

The photocatalytic degradation efficiency of the catalyst is also affected by the amount of catalyst in the solution. As the quantity of the catalyst increase, the number of active sites on the semiconductor surface also increase with the increment of the amount of the $OH^{\cdot -}$ and $O_2^{\cdot -}$ produced which leads to enhancement of photocatalytic degradation [56]. However, the increment of the catalyst beyond its optimum amount hinders the reaction rate because there might be decrease in the light penetration depth into the solution and diminish light scattering [56].

2.2.2.2.6. Concentration of pollutant in wastewater

Another factor, which determines the degradation efficiency of the photocatalysis reaction, is the type of pollutants and their concentration. photocatalytic activity under similar operating condition using similar catalyst with variation in the preliminary concentration of water contaminant results in different degradation efficiency [55]. S.Nahar *et al*. studied the effect of the Rhodamine B concentration on the photocatalytic performance of Ag/Ag_2SO_3 by utilizing different concentration of Rhodamine B in the range of the 5-20 mg/L. The photocatalytic performance of Ag/Ag_2SO_3 decrease from 99 % to 1 % when the concentration of the Rhodamine B changed from 5 to 200 mg/L. This may be due to two reasons, the first one is the excessive absorption of Rhodamine B on the surface of photocatalyst and the second one is the increasing of the dye concentration which decrease the transmission of the experimental solution and also can lead to reduction of amount of photons reaching the catalyst surface [31].

2.2.2.3. Photocatalysts

Recently, research works are focused on the semiconductor based photocatalysis for removal of organic and inorganic contaminants from aqueous and gas phase system for the environmental cleanup, water treatment and industrial and health application [67-71]. Semiconductors are preferable for photocatalysis due to their unique electronic properties, the filled valence band and empty conduction band, response to the light energy by moving the electron from the valence band to conduction band which is equal to their band gap energy [36]. TiO_2 [12, 13] and ZnO [14-17]

semiconductors are extensively studied. Titanium oxide is widely used due to its non toxic, thermodynamic stability and high oxidizing power [12]. Moreover, zinc oxide is used as alternative material to TiO_2 with high photocatalytic activity [72]. However, the absorption of TiO_2 and ZnO is in the UV region of the solar radiation, which is only 5% of the solar energy and cover small content of the solar radiation when compared to the visible (43%) and infrared ray (52 %) [73]. In spite of this, they are affected by recombination of electron and hole during irradiation [72, 74]. To enhance the performance of the photocatalyst doping with metal, nonmetal and coupling of the semiconductor with each other and metal was done as many research work shows [5, 14, 15, 74-77].

2.2.2.3.1. Doping of semiconductors with metal and nonmetals

Doping of the semiconductor by nonmetal, metal and transition metal is a simple method that enhances the photocatalytic performance of the semiconductor by inhibiting the charge carrier recombination and increasing the specific area of the semiconductor material [78, 79]. Moreover, visible light absorption is enabled by defect state created in the band gap of the semiconductor during the doping process [79]. Rapid charge carrier recombination is inhibited and the interfacial charge transfer is enhanced by the trapping of valance band VB holes and conduction band (CB) electrons in the defect state to the CB or from the VB to the defect states are allowed under sub band gap irradiation [80-83].

Among the doping mechanism, metal ion doping is preferred since the metal dopant has potential to transfer electrons and decrease the band gap energy level of the semiconductor. In addition, they are activated in the presence of light source and generating electrons [78, 84-90]. Wen Ting *et al*. synthesized Ba- doped Bi_2WO_6, which exhibit high photocatalytic performance as a result of the surface area increased, the crystalline size decreased and the electrons are trapped by the Ba, which leads to the separation of electron-hole [84]. Moreover, metal ions dopants such as; (Ag, Mo, Fe, Au, Co, Zn, Al, Ni, Ti, and Cu) are doped into the semiconductor photocatalyst to enhance the photocatalytic performance [78, 84-90]. Furthermore, S, N, B, P and F nonmetals dopant can be enhance photocatalytic performance of the pristine material by extending the absorption to the visible region [80-83]. Among this doping, sulfur (S) doping is more preferable due to the high thermal stability and significantly enhances the photocatalytic activity under the visible light [81, 91, 92]

2.2.2.3.2. Heterojunction photocatalysis

Like doping, the p-n junction formation enhances the photocatalytic performance by suppressing the charge recombination, which is due to the built in electric field between the p-type and n-type semiconductors [14, 23, 26, 93-95]. As indicated in Figure 2.6 the electric field or depletion region is formed when the electron flow from the conduction band of n-type semiconductor to conduction band of the p-type semiconductor and the holes also flows from the valence band of the p-type semiconductor to the valence band of the n-type semiconductor [24, 25]. J Zhu *et al*. synthesized novel Cu_2O@$HNbWO_6$ Via solution redox method which exhibit excellent photocatalytic performance over MB degradation [96]. Also R Jio *et al*. synthesized Co_3O_4/MoS_2 photocatalyst by hydrothermal method for efficient removal of 2-Mercaptobenzothazole and tetracycline under visible light [97]. In addition to this, many works have done on the heterojunction photocatalyst, which enhance the photocatalytic performance [14, 44, 74, 98-100].

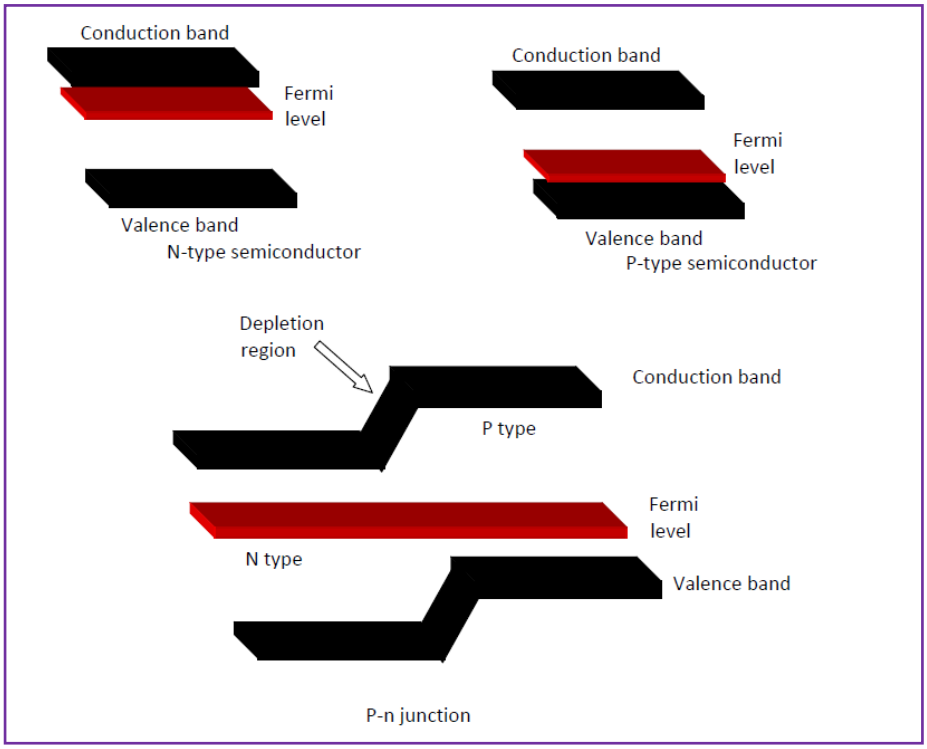

Figure 2.6 Schematic representation of the electronic structure of p, n and p-n junction semiconductors

2.3. Zinc ferrite based photocatalyst

Spinel ferrites, which have a novel property, with unusual magnetic, electric and optical properties associated to the nano-scale make them suitable for high frequency transformers, magnetic recording media, telecommunications and biomedical application [23, 93, 94]. Among this ferrite zinc ferrite become the promising visible light photocatalyst with magnetic separation properties, low cost, photochemical stability and non-toxicity [21]. Zinc ferrite has a spinel crystal structure in which the octahedral and tetrahedral site is occupied by Fe^{3+} and Zn^{2+} respectively [101]. The distribution of the zinc and iron cation in the tetrahedral and octahedral site in the nanoparticles and the size of the particle affect the magnetic property [87]. The magnetic behavior changes from the antiferromagnetism to ferromagnetism when the zinc ferrite changed from the bulk to the nanoscale [87].

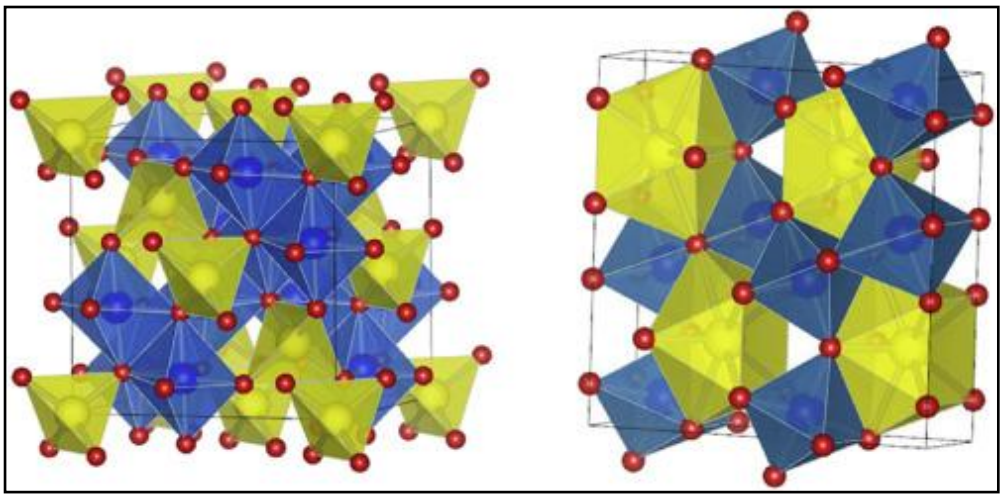

Figure 2.7 Crystal structure of zinc ferrite [101]

Zinc ferrite has suitable band position and band gap, which has adverse effect on the photo catalysis. H.Guo *et al*. reported as the valence band position of the zinc ferrite is 0.83 eV/NHE and the conduction band position is -0.98 eV/NHE [22]. Moreover, $ZnFe_2O_4$ has narrow band gap (E_g = 1.72-2.1 eV) in the range of visible [22, 102]. However, the photocatalytic activity of this ferrite is limited by the rapid charge recombination [2]. Coupling of the $ZnFe_2O_4$ with other semiconductor [26, 103-106], noble metal [107] and Plasmon integrated semiconductor [2, 28, 29, 108, 109] suppress charge recombination due to the schottky barrier formed at the metal-semiconductor interface.

Among them, the p-n junction formation is best way to enhance the photocatalytic performance by suppressing the charge recombination, which is due to the built in electric field between the p-

type and n-type semiconductors [14, 23, 26, 93-95]. The n-type $ZnFe_2O_4$ coupled with other semiconductors to decrease the charge recombination for the enhancement of the photocatalytic performance as shown in Table 1 [22-26]. From the p-type semiconductor the Ag_2O form a good interface with the $ZnFe_2O_4$ and the formed heterojunction has good photocatalytic performance under visible light irradiation [22] F.shin *et al.* synthesized $Ag_2O/ZnFe_2O_4$photocatalyst which exhibit a complete degradation of (methyl blue, methyl orange, Rhodamine B and phenol with 50 minutes and 8 minutes respectively [25]. However, the concentration of silver used is high (60%) which leads to the increment of production cost. Further, it reduce the recoverability capacity of the nonmaterial [25]. Additionally, H.Guo *et al*. demonstrate the effect of Ag_2O loading on the photocatalytic performance of $ZnFe_2O_4$, high amount loading decrease the photocatalytic performance by shielding the active site in $ZnFe_2O_4$, likewise photocatalytic performance decrease during low amount loading by increasing charge carrier recombination [22]. Therefore, further work is required to increase the photocatalytic performance of $Ag_2O/ZnFe_2O_4$ photocatalyst by simultaneously increasing the active site and decrease the charge carrier recombination rate without reducing the recoverability of the photocatalyst.

Table 1 Coupled zinc ferrite with other p-type semiconductors.

Photo-catalyst	Synthesis method	Pollutant	Degradation efficiency	Refer ence
p-BiOCl/n-$ZnFe_2O_4$	Facile solvothermal	Rhodamine B (RhB)	87% within 180 min	[23]
p-AgI/ n-$ZnFe_2O_4$	Facile one step hydrothermal	Rhodamine B (RhB)	98.5% within 40 min	[24]
P-Ag_2O/n-$ZnFe_2O_4$	Facile deposition precipitation	Bisphenol A	92.5% within 60 min	[22]
p-Ag_2O/n-$ZnFe_2O_4$	Simple precipitation	Phenol and Rhodamine B	Complete decomposition within 18 and 50 min respectively	[25]
p-Bi_2MoO_6/ n-$ZnFe_2O_4$	Electro spinning combined with solvothermal	Rhodamine B	88.97% within 240 min	[26]

The integration of the Plasmon metal nano-particles into the heterojunction photocatalyst increases the photocatalytic performance by suppressing the electron-hole recombination and extending the absorption to the visible region and in some cases to the infrared [5, 49, 77, 110]. Moreover, enhance the photocatalytic performance of the substrate by transferring the generated hot electrons in the surface of the Plasmon particle and serve as antenna for light absorption [13, 31, 111]. Furthermore, plasmonic Ag can be used to enhance the photocatalytic performance of $ZnFe_2O_4$ based heterostructure semiconductor as indicated in Table 2. No report is seen still now in the Plasmonic Ag integrated P-Ag_2O/n-$ZnFe_2O_4$. $Ag_2O/ZnFe_2O_4$ photocatalyst performance declined due to limited active site when the Ag_2O deposited [22]. Green synthesis method yields small sized particle with high specific surface area.

Table 2 Plasmon silver integrate coupled zinc ferrite

Photo catalyst	Synthesis method	Pollutant type	Degradation efficiency	Reference
$Ag/AgBr/ZnFe_2O_4$	Deposition precipitation	Rhodamine B	98% in 300 minutes	[27]
$Ag/AgCl/ZnFe_2O_4$	Facile hydrothermal and deposition precipitation	17α-ethylestradiol	Complete in 240 minutes	[28]
$ZnFe_2O_4/Fe_3O_4/Ag$	Sol-gel combined with electrospinning	Methyl blue and methyl orange	75% in 120 minutes	[29]
$ZnO/ZnFe_2O_4/Ag$	Layered by layered	Dichlorophenol	97.9% in 75 minutes	[2]
$ZnFe_2O_4/Ag/Ag_3VO_4$	Two step hydrothermal	Methyl orange	81% in 32 minutes	[109]

Recently, synthesis of nanoparticle by green synthesis or biosynthesis is preferable than other chemical and physical methods due to its one step process, cost effective, environmental friendly and frequently lead to preparing more stable materials, relatively reproducible and small sized

nanoparticles [112-116]. For the biosynthesis of nanoparticles, natural reagents such as microorganisms as reducing and capping agent, fruits, marine algae, sugars, plant parts (roots, seed, leaf, steam and latex) are used [112-115]. Plants is more preferable due to the coexistence of different biomolecules; such as bioactive flavonoids, polyphone, phenolic acids, protein, terpenoids, carbohydrate, fats, amino acids, gum, polysaccharides, alkaloids, alcoholic compounds, proteins, enzymes and vitamins. These biomolecules playing a significant role in reducing the metallic ions first and then acting as a capping or chelating agent due to the structural arrangement constraints [112-115]. However, only few researches have been done on the synthesis of $ZnFe_2O_4$ by the biosynthesis method (Table 3).

Table 3 Green synthesized zinc ferrite

Synthesis method	Green material	Calcinations temperature (^{o}c)	Morphology	Reference
Modified sol gel	Aloe Vera extract	900	Agglomerated	[117]
Combustion	Sugarcane juice	600	Spherical	[118]
Green	*Moringaoleifera*	700	Agglomerated	[119]
Conventional heating	*Opuntiadillenii haw*	900	Spherical	[120]
Microwave heating	*Opuntiadillenii haw*	-	Spherical	[120]
Microwave assisted combustion	*Hibiscus rosasinesis*	900	Nanoparticle	[102]
Combustion	*Hibiscusrosasinesis*	-	Nanoparticle	[102]
Solgel combustion	Honey mediated	1000	Spherical	[121]
Microwave assisted green synthesis	*Limoniaacidissima juice*	600	Spherical	[114]
Green	*Aeglemamelos leave extract*	900	Spherical	[115]

The photocatalytic performance of biosynthesized $ZnFe_2O_4$ was also studied by using different organic dyes [114, 118]. In 2018 S.B. Patil *et al*. synthesized sugarcane mediated $ZnFe_2O_4$ for the degradation of mixed dyes which degrade 98% methyl blue and 95% of rose Bengal in 120 min with irradiation of UV visible radiation [69]. Green synthesized $ZnFe_2O_4$ photocatalyst was studied rarely for wastewater treatment.

Here in, a new plant type *Ajuga intergrafolia* (Harma gusa (Afan oromo name)) is proposed as stabilizing and capping agent for the synthesis of $ZnFe_2O_4$ because it contains a bioactive molecule such as flavonoids, phenolic acids, saponins, steroidal and tannins compounds that used as chelating agent due the hydroxyl radical content [122-124]. This plant was used as traditional Ethiopian medicine plant for treatment of different disease such as diabetes, malaria, skin disease, high blood pressure, stomach pain, pneumonia, liver problem due to its high antioxidant property of the plant constituents [122, 123, 125]. So this plant can be used as a capping/stabilizing agent for the green synthesis of $ZnFe_2O_4$. The plant was extracted for the synthesis $ZnFe_2O_4$ to serve as a capping/stabilizing agent.

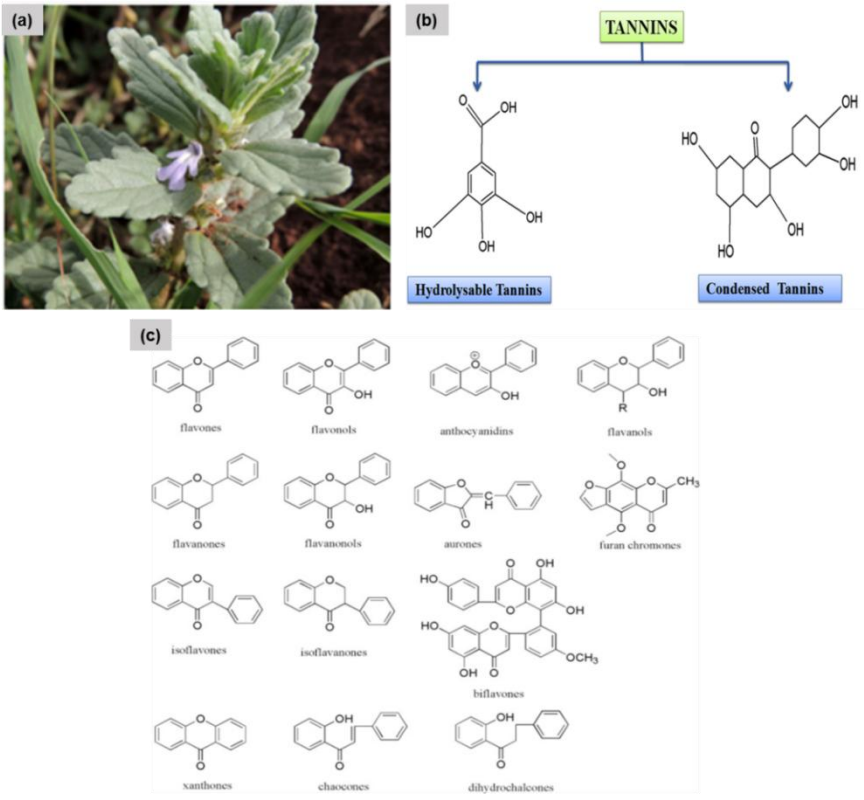

Figure 2.8 Picture of *Ajuga integrafolia* (Harma gusa) plant (a) and chemical structure and classification of (b) Tannins and (c) Flavonoids [122]

CHAPTER THREE

3. Methodology

3.1. Materials and Chemicals

The chemicals utilized in this thesis work include Zinc chloride ($ZnCl_2$), silver nitrate ($AgNO_3$), Iron chloride hexahydrate ($FeCl_3.6H_2O$), Hydrochloric acid (HCl) and Sodium Hydroxide (NaOH), Ethanol and all are purchased from Loba Chemicals Reagent Company. Whatman no one filter paper was also used for filtration. Moreover, the plant leave of *Ajuga integrafolia* (Harma gusa) was collected from Gura forest around Gedo town, West Showa zone, Oromia region, Ethiopia.

3.2. Methods

This part contain all the procedure carried out to obtain $Ag/Ag_2O/ZnFe_2O_4$ composite by integrating Ag into $Ag_2O/ZnFe_2O_4$ by calcination and evaluating the photocatalytic performance towards Methylene Blue (MB) dye.

3.2.1. Extraction of plant

The collected *Ajuga intergrafolia* plant leave was washed several times with distilled water to remove unwanted and dirt substance from the leave, followed by drying in oven for 24 hr at 60 °C. Then grinded to obtain powder and 15 g of the powder was dissolved in 450 ml of distilled water, followed by boiling at 50 °C for 1 hr. Finally, the boiled solution was filtered by using Whatman number one filter paper and the extracted solution was used as *Ajuga integrafolia* extract solution that contains bioactive molecules such as Tannins, Flavonoids, Saponins, Phenolic compounds and so on [119, 125].

3.2.2. Synthesis of $ZnFe_2O_4$

For the synthesis of $ZnFe_2O_4$, green synthesis method was used due to the advantages of size and shape control of $ZnFe_2O_4$ powders. Stoichiometeric ratio 1:2 of the $ZnCl_2$ and $FeCl_3.6H_2O$ was dissolved in 50 ml of distilled water separately. The prepared solution was added drop wise to 100 ml of plant extract solution with continuous stirring for 30 minute using hot stirrer to obtain a uniform solution consecutively. Then, 0.5 M sodium hydroxide solution was added into the solution until the pH of the solution reach 12 and the temperature was increased from room

temperature to 80 °C. The obtained suspension was washed several times using distilled water and ethanol. Finally, the dried powder was calcined at different temperatures (500, 600, 700, 800, 900, 1000 and 1100 °C) for 2 hr with 10°C/min heating rate and denoted as ZW (zinc ferrite with a plant extract) followed by numbers of 5, 6, 7, 8, 9, 10, and 11, respectively, where the numbers indicate the calcination temperatures [114, 121]. These calcination temperatures were obtained from Thermo-gravitometric analysis (TGA). The calcinations were performed to determine the temperature at which the single phase of $ZnFe_2O_4$ is formed. The single phase of $ZnFe_2O_4$ was formed at a temperature of 1000 °C, i.e., ZW-10. For comparison, $ZnFe_2O_4$ synthesized by a chemical synthesis route following all the above procedure except the utilization of the plant extract and named as ZWO (zinc ferrite without plant extract).

3.2.3. Synthesis of $Ag_2O/ZnFe_2O_4$

To synthesis the $Ag_2O/ZnFe_2O_4$, facile deposition-precipitation method was used. First 1 g of as synthesized $ZnFe_2O_4$ (ZW-10) was dissolved in 50 ml of distilled water, which was subjected to sonication for 30 min to obtain a uniformly distributed suspension. After that, stoichiometeric volume of 0.1M NaOH was dissolved into the suspension by continuously stirring for 1hr, until a uniform suspension was obtained. The stoichiometeric volume of 0.1M $AgNO_3$ was slowly dropped into the suspension and the resulting mixture was kept stirred for another 4hrs in the darkness. Finally, the product was washed and centrifuged several times, followed by drying at 80°C overnight [22]. The composite with different percentage was synthesized to obtain the composite with optimum photocatalytic performance. The naming used for the composite, i.e., the designation systems of the composite of Ag_2O and $ZnFe_2O_4$ is summarized and reported in the following Table 4. The naming is in such a way that AZW-1 for example, stands for the composites of Ag_2O and $ZnFe_2O_4$ synthesized with plant extract (ZW), and the number '1' stands for the sample with 5% that is AZW-1, and so on. Ag_2O (A) was synthesized for the comparison by slowly dropping 0.1 M $AgNO_3$ dissolved in 30 ml into 0.1 M NaOH dissolved in 60 ml by continuously stirring. Then the suspension was washed several times with water and final dried overnight at 80 °C.

Table 4 Percent of composition of Ag_2O and $ZnFe_2O_4$ with its corresponding designation systems.

Name of samples	Percent of composition
AZW-1	Ag_2O(5%) and $ZnFe_2O_4$(95%), i.e., 5% Ag_2O/95% $ZnFe_2O_4$
AZW-2	Ag_2O(10%) and $ZnFe_2O_4$(90%), i.e., 10% Ag_2O/90% $ZnFe_2O_4$
AZW-3	Ag_2O(15%) and $ZnFe_2O_4$(85%), i.e., 15% Ag_2O/85% $ZnFe_2O_4$
AZW-4	Ag_2O(20%) and $ZnFe_2O_4$(80%), i.e., 20% Ag_2O/80% $ZnFe_2O_4$

3.2.4. Synthesis of $Ag/Ag_2O/ZnFe_2O_4$ and calcination temperature effect

First, 1 g of as synthesized $ZnFe_2O_4$ (ZW-10) was dissolved in 50 ml of distilled water, followed by 30 minutes sonication to obtain uniform suspension. After that, stoichiometeric volume of 0.1 M NaOH was dissolved in the suspension for precipitating the solution, followed by continuous stirring for 1hr until uniform suspension was obtained. Then, stoichiometeric volume of 0.1 M $AgNO_3$ was slowly dropped into the suspension with continuously stirring for about 4hr. The suspension was washed with water several times. Then the washed suspension was dried at 80 °C overnight. Final the dried powder was subjected to calcination at 280 °C for 1 hr [42]. The composite with different composition was synthesized for optimization. The following Table 5 shows the percentage composition of the $Ag/Ag_2O/ZnFe_2O_4$ material.

Table 5 Percent of composition of silver/silver oxide and zinc ferrite with its naming.

Name of samples	Percent of composition
AAZW-1	(Ag/Ag_2O) (5%) and $ZnFe_2O_4$ (95%), i.e., 5% (Ag/Ag_2O)/95%$ZnFe_2O_4$
AAZW-2	(Ag/Ag_2O) (10%) and $ZnFe_2O_4$ (90%), i.e., 10% (Ag/Ag_2O)/90% $ZnFe_2O_4$
AAZW-3	(Ag/Ag_2O) (15%) and $ZnFe_2O_4$ (85%), i.e., 15% (Ag/Ag_2O)/85% $ZnFe_2O_4$
AAZW-4	(Ag/Ag_2O) (20%) and $ZnFe_2O_4$ (80%), i.e., 20% (Ag/Ag_2O)/80% $ZnFe_2O_4$

The above samples were optimized of their photocatalytic degradation performances towards the MB and the sample with the composition of 15%(Ag/Ag_2O)/85% $ZnFe_2O_4$ was an optimum sample. Moreover, the effect of the calcination temperature on the optimum composite was investigated towards the formation of Ag from Ag_2O by changing the temperature, i.e., 260 °C,

280 °C and 300 °C. The calcination was performed on the sample with a composition of 15% (Ag/Ag_2O)/85% $ZnFe_2O_4$ as this sample showed an optimum degradation performance. Depending on the calcination temperatures, the calcined composite was denoted by AAZW-3-1, AAZW-3-2, and AAZW-3-3, respectively, with their calcination temperatures of 260 °C, 280 °C, and 300 °C, respectively.

3.3. Characterizations

For thermal analysis study and determination of temperature at which the $ZnFe_2O_4$ is formed, we used thermogravimetric–differential thermal analyzer (TGA - DTA) (SHIMADZU DTG-60H). The crystal structure and phase composition (phase purity) of the as synthesized samples were determined by using XRD (SHIMADZU XRD -7000), in the 2θ range of 10 – 80º generated by voltage of 40 kv and filament current 30 mA radiating $CuK\alpha_1$ radiation (λ= 1.5418 A). Fourier transform infrared (FTIR) (FT/IR-6600 type A) was used to analysis chemical composition of the samples in the wave number range of 400-4000 cm^{-1}. Additionally, the microstructure, morphologies, and elemental composition analysis of the samples were analyzed by using Scanning Electron Microscopy/Energy Dispersive Spectroscopy (SEM/EDS), (COXIEM-30). UV-visible spectroscope (UV-3600Plus) was used to measure the absorbance of the MB dye after photocatalytic experiment.

3.4. Photocatalytic activity study

The photocatalytic performance of the synthesized samples was evaluated by irradiating the visible light (150-Watt Halogen lamp) and using methylene blue (MB) as an organic dye. About 25 mg of catalyst was added into 10 part per million (ppm) of 125 ml solution of MB. Then, the solution was sonicated for about 30 min in the dark to achieve adsorption-desorption equilibrium between a catalyst and pollutant. After the establishment of an equilibrium, the 150 W Halogen lamp visible light was irradiated to the suspension with a continuously stirring. Then, a sample was taken from the suspension within 20 min time interval. Finally, the concentrations of residual pollutant were measured using UV-visible spectroscopy to obtain the concentration (C_t) from the absorbance against wavelength plot, according to the Beer Lambert law, given in the following equation (1).

$$\mathbf{A = \varepsilon b C_t} \ldots\ldots\ldots\ldots\ldots\ldots\ldots\ldots \quad (1)$$

Where, **A** is absorbance, **ε** is absorbitivity, and C_t is the concentration of the MB after a time ***t***.

Moreover, the effects of the pH on the degradation efficiency were studied by adjusting the pH of the MB using 0.1M HCl and 0.1M NaOH solution, for acidic and basic media, respectively. The effects of the pH of the MB were carried out in acid, neutral, and basic regions by fine-tuning the pH to 4, 7, and 10, respectively.

CHAPTER FOUR

4. Results and discussion

4.1. Thermal analysis

The TGA-DTA of zinc ferritewith and without plant extract are shown in the Figure 4.1(a) and (b), respectively. The TGA results indicate that zinc ferrite sythesized with plant leave extract showed around 15% of mass reduction, while zinc ferrite without the plant extract showed a mass reduction of about 15.51%. This could be related to the removal of physisorbed water and organic matter in the plant extract for the plant templated zinc ferrite and oxidative decomposition of precursor [126]. The endothermic peak around 70 – 120 °C in the DTA of zinc ferrite without plant extract (Figure 4.1(a)), indicates the removal of physisorbed water molecules. Other endothermic peaks around a temeprtaure of 180 – 220 °C and 280 – 320 °C corresponds to the oxidative decomposition of the precursor [126, 127]. The DTA graph of the zinc ferrite with plant extract sample, (Figure 4.1(b)), shows an endothermic peak around 70 – 100 °C, which could be related to the loss of physisorbed water molecules. Additionally, the peak around 180–320 °C is exothermic peak showing the removal of organic compounds from the plant extract, which is in a close agreement to the previous work by Ranjit *et al.*of zinc ferrite TGA-DTA analysis [127]. Furthermore, endothermic and exothermic peaks, simultaneously, appear in the TGA-DTA above 400 °C, which may be related to the crystal lattice rearrangement within the samples and movement of iron cations from the octahedral to tetrahedral site [126].

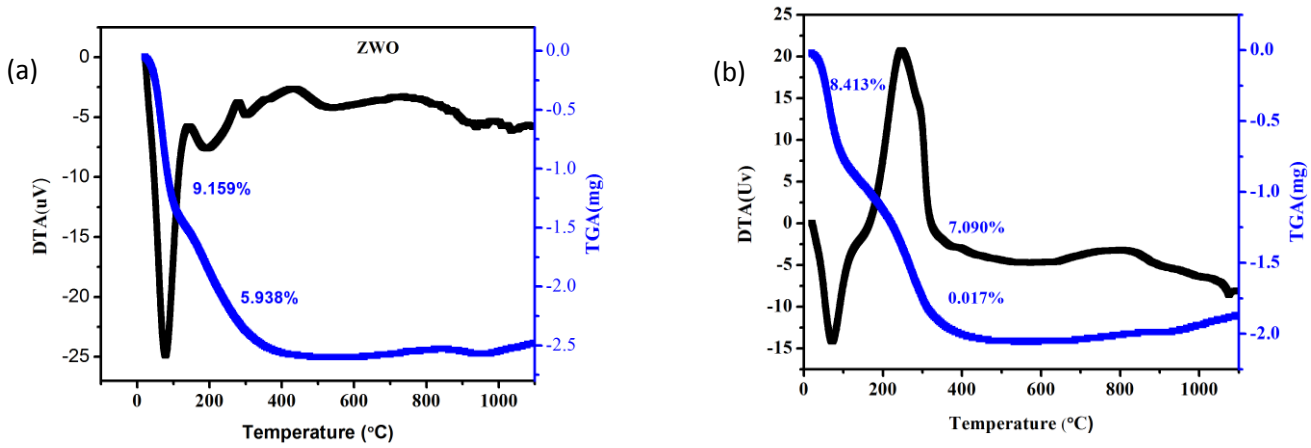

Figure 4.1 TGA-DTA graph of chemical synthesized zinc ferrite without plant extract (a) and green synthesized with plant extract (b).

Because of variety of complex reaction in the formation of spinel-structured oxides, it is necessary to know the mechanism of formation of spinel structured $ZnFe_2O_4$. The cation diffusion phenomena at elevated temperatures can lead to the formation of zinc ferrite [126]. A Cationinter-diffusion coefficient in the ferrite phase is larger than the diffusion coefficient of the cations in the metal oxide (ZnO and Fe_2O_4) at the intermediate temperature of about 400 ºC. Therefore, the meta stable phase formation of gamma iron is possible and transition between gamma and alpha iron oxide accompanied by the diffusion of Zn ions into the lattice, yield the formation of spinel structured zinc ferrite ($ZnFe_2O_4$) [126].

4.2. XRD analysis

The XRD pattern of all as synthesized samples is presented in the following Figure 4.2(a-d). Figure 4.2(a) shows the diffraction pattern of synthesized zinc ferrite with plant extract exhibiting diffraction peaks at 2θ of 18.2°, 29.7°, 35.7°, 36.8°, 42.8°, 53.0°, 56.5°, 62.0°, 70.4°**,** and 77.2°, which were indexed to crystallographic planes of, respectively, (111), (220), (311), (222), (400), (422), (511), (440), (533), and (622), and similar to JCPDS -22-1012 [128]. However, there is additional peak at 2θ of 31.8º in the XRD pattern of ZW-5, ZW-6, ZW-7 and ZW-8 samples, which indicates the presence of ZnO (JCPDS – 36-1451) [129]. Moreover, the peak at 2θ of 33.2º, in the XRD pattern of ZW-8, ZW-9, ZW-7, and ZW-11 indicates existence of impurity phase Fe_2O_3 that matches JCPDS: 33-0664 [105]. Furthermore, the additional peaks shown in the XRD pattern of ZW-5, ZW-6, ZW-7 and ZW-8 at 2θ = 49.5° indicates the presence of Fe_2O_3 impurity phase that matches with JCPDS: 33-0664 [105]. Therefore, only the sample calcined at 1000°C (ZW-10) shows the formation of pure phase spinel structured $ZnFe_2O_4$.

As shown in the Figure 4.2(b), the diffraction angles at 2θ of 32.8°, 38.2°, 54.9 and 66.2° of as synthesized Ag_2O indicated as (A) on the diffraction pattern showed crystallographic planes of (111), (200), (220), and (311), respectively, which is in an agreement with cubic structure Ag_2O (JCPDS card number: 41-1104) [22, 130]. The XRD pattern of all synthesized $(x)Ag_2O/(1-x)ZnFe_2O_4$ (x = 0.05, 0.1, 0.15 and 0.2), designated as AZW-1 up to AZW-4 on the graph, confirmed that both Ag_2O and $ZnFe_2O_4$ exist in the composite samples. The Ag_2O peak shown at 32.9° and 38.2° represents the (111) and (200) plane of its cubic structure of Ag_2O (JCPDS card number: 41-1104) [22, 130], while the peaks at 2θ of 18.2°, 29.7°, 35.7°, 36.8°, 42.8°, 53.0°, 56.5°, 62.0°, 70.4° and 77.2° indicating the existence of the cubic spinel $ZnFe_2O_4$ as shown in the Figure 4.2

(b) [128]. The existence of all diffraction peaks of Ag_2O and $ZnFe_2O_4$ in all samples with no significant shift in the peaks indicate that the introduced Ag_2O is not incorporated into the crystal structure of $ZnFe_2O_4$. Figure 4.2(c) presents the XRD patterns of the calcined samples at a temperature of 280 °C of the composites of (x) Ag_2O/(1-x) $ZnFe_2O_4$(x = 0.05, 0.1, 0.15 and 0.2) showing coexistence of Ag_2O and $ZnFe_2O_4$. In the calcined (x)Ag_2O/(1-x) $ZnFe_2O_4$(x = 0.05, 0.1, 0.15 and 0.2) composites, the additional peak is observed at 2θ of 44.2° on XRD pattern AAZ-4 of Figure 4.1(c) and AAZW-3-3 of Figure 4.2(d), corresponding to the (200) planes of Ag with card number of JCPDS-4-0783 [129]. However, the Ag peak is not visible in the XRD pattern of sample AAZW-1, AAZW-2, and AAZW-3 of Figure 4.1(c), and AAZ-3-1 of Figure 4.2(d), which could be due to the complete dispersion of the Ag in the composite, according to the Hai Gue *et al*. mentioned in his work [42].

The characteristic peak of Figure 4.2(c) at 2θ of 32.9°, 38.2°, 54.9° and 66.2° on the XRD pattern of calcined AAZW-4 composite sample is related to the crystallographic planes (111), (220) and (220), respectively, of Ag_2O in an agreement to the JCPDS with card number: 41-1104 [22, 129, 130]. Moreover, the XRD pattern of AAZW-2 and AAZW-3 indicate the existence of Ag_2O at 2θ of 32.9° and 38.2° [22, 129, 130]. In the AAZW-1 XRD pattern, the existence of Ag_2O confirmed by the peak presented at 2θ of 32.9°. Furthermore, the entire diffraction peak originated from $ZnFe_2O_4$ in the composite maintained as it is and there is no significant shift of the diffraction peaks, that indicates both Ag and Ag_2O is not incorporated into the crystal structure of $ZnFe_2O_4$.

The XRD pattern of as synthesized Ag/Ag_2O composite (Figure 4.2(c)) shows the existence of both Ag and Ag_2O. At 2θ of 44.2° and 77.4° diffraction peaks correspond to crystalline planes of (220) and (311) of Ag (JCPDS-4-0783), respectively, while the peak at 2θ of 32.9° and 38.2° correspond to the crystalline planes of (111) and (200) of Ag_2O (JCPDS card number: 41-1104), respectively [22, 129, 130].

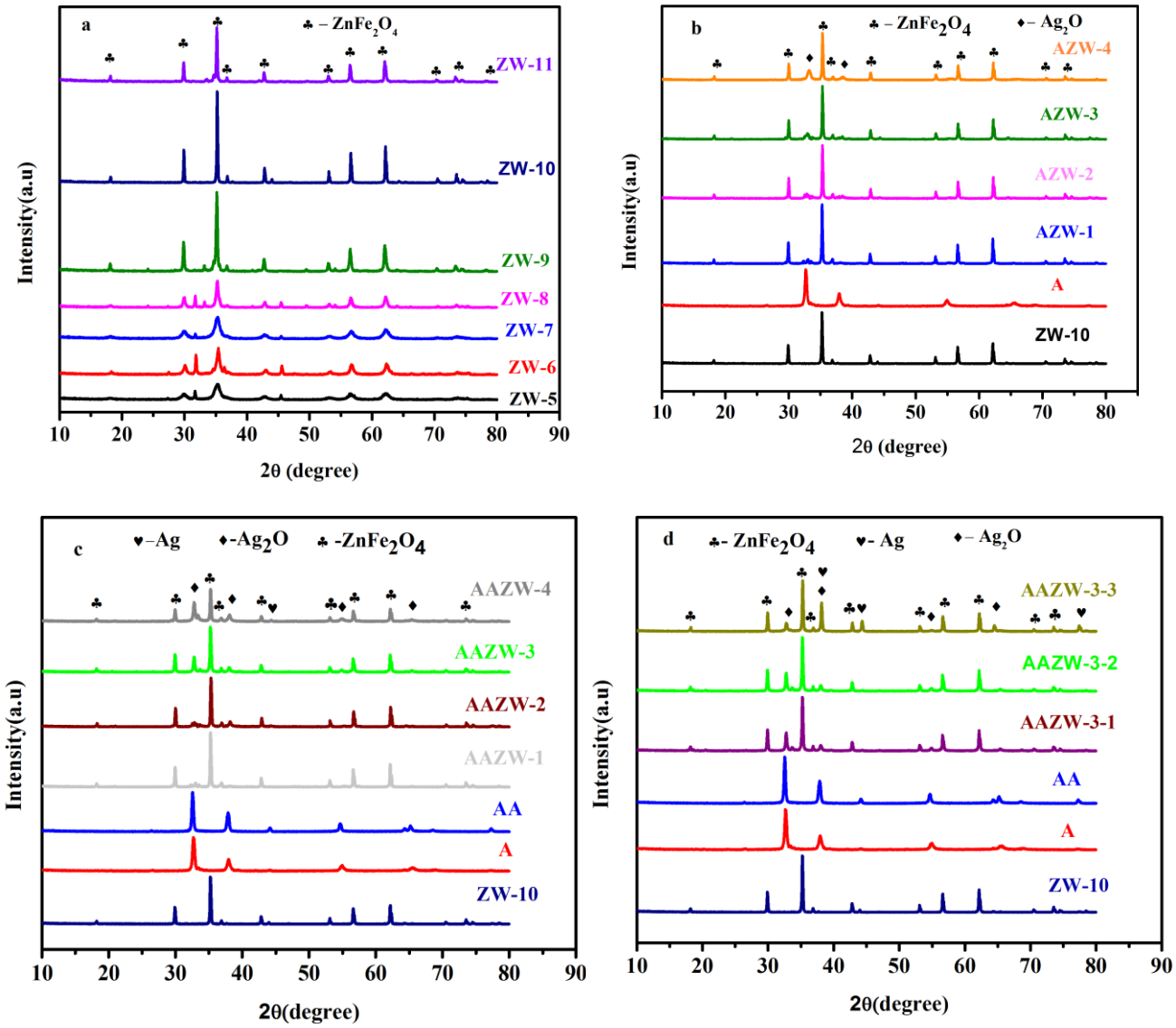

Figure 4.2 XRD pattern of synthesized samples of zinc ferrite with plant extract (ZW-5 up to ZW-11), calcined in a temperature range from 500–1100 °C, (a), As-synthesized $Ag_2O/ZnFe_2O_4$ composites, (b), Ag2O/ $ZnFe_2O_4$ composites subjected to calcination at a temperature of 280 °C, (c), and 15wt% of Ag_2O in $ZnFe_2O_4$ subjected to calcination temperature of 260, 280 and 300 °C, (d).

The crystalline size of the synthesized sample was calculated using scherrer equation [131], as given below.

$$\mathbf{D} = \frac{0.89\lambda}{\beta \cos\theta}$$

where *D* is average crystalline size, **λ** denotes X-ray wavelength (0.1542 nm), **β** is the full width at half maximum (FWHM) and **θ** represents the Braggs angle corresponding to the reflection plane [131]. The following table summarizes the average crystalllite size for each of the samples.

Table 6 The calculated crystalline size.

Sample name	**Average crystalline size (nm)**
ZW-5	8.258
ZW-6	18.62
ZW-7	19.44
ZW-8	21.32
ZW-9	34.36
ZW-10	50.15
ZW-11	51.51
ZWO	57.51
A	19.4
AA	25.81
AZW-1	60.08
AZW-2	57.86
AZW-3	55.11
AZW-4	55.17
AAZW-1	58.89
AAZW-2	56.82
AAZW-3	50.01
AAZW-4	49.17
AAZW-3-1	49.81
AAZW-3-3	56.58

The reduction in the crystalline size of $ZnFe_2O_4$ (ZW-10) calcined at 1000 ºC is due to the capping/ stablizing agents in the plant leave extract when compared to as synthesized $ZnFe_2O_4$ (ZWO) sample controlling the crystal growth [112-116]. This suggests that the performance of the

sample of ZW-10 could be enhanced compared to that of the ZWO. The crystalline size of the $Ag/Ag_2O/ZnFe_2O_4$ particle increases with increasing of the calcination temperature as shown in the Table 6 that indicates the effect of the calcination for the formation of Ag aggregate the Ag that further lead to the shielding of the active site in the $ZnFe_2O_4$ [107, 132]. Furthermore, both uncalcined and calcined composite materials show the decrease in crystalline size when the percentage loading of Ag_2O and Ag/Ag_2O increase which indicate the deposition covers the $ZnFe_2O_4$ [27]. The crystalline size of Ag/Ag_2O loaded $ZnFe_2O_4$ composite is lower than that of the corresponding Ag_2O loaded $ZnFe_2O_4$ comosite this may due to the loading of Ag/Ag_2O cover the $ZnFe_2O_4$ than that of it comparative Ag_2O [27].

4.3. FTIR analysis

FTIR spectra of uncalcined and calcined $ZnFe_2O_4$ (ZW-10) are presented in the Figure 4.3 below. The characteristic absorption peak at wavelength of 460 cm^{-1} and 520 cm^{-1} are the Zn-O and Fe-O bond intrinsic lattice vibration of $ZnFe_2O_4$ [133, 134]. The strong broad characteristic absorption at 3280-3420 cm^{-1} (centered at 3450 cm^{-1}) indicate the existance of O-H bond stretching from a free adsorbed water molecule [135]. The sharp peak at 1643 cm^{-1} corresponds to the O-H bending vibration of O-H group [126, 136]. Moreover, there are peaks at 1114 cm^{-1} which implies as there is carbon dioxide adsorbed on the surface [114]. This result confirm as $ZnFe_2O_4$ formed effectively by green synthesis route.

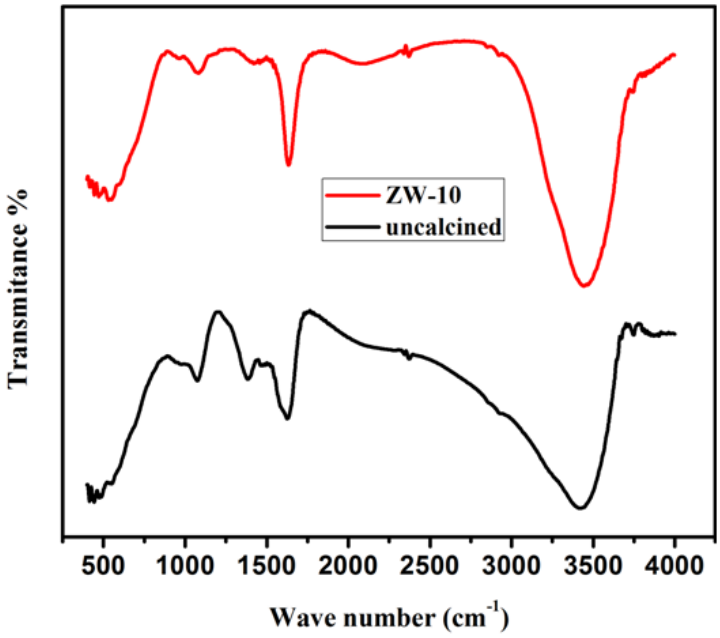

Figure 4.3 FTIR spectrum of green synthesized $ZnFe_2O_4$ uncalcined and calcined at 1000 ºC

4.4. SEM /EDS analysis

As shown in Figure 4.4(a1), The SEM image of as synthesized Ag_2O shows nearly spherical aggrigated particles. The ZWO shown the agglomerated plate like particleas as SEM image in Figure 4.4(b1) shows. Moreover, Figure 4.4(c1) shows the formation of spherical shaped Ag/Ag_2O. Furthermore, the green synthesized ZW-10 SEM image indicates as the agglomerated plate like particles are formed as shown in the Figure 4.5a, which is well distributed than the ZWO. In Figure 4.5a and c the AZW-3 and AAZW-3 composite SEM image more particle distributed than ZW-10 which indicates well deposition of Ag_2O and Ag/Ag_2O in the surface of the $ZnFe_2O_4$ [22]. Complemeter EDS study was carried with SEM. Figure 4.4(a2) and 4.5c shows the EDS analysis of A that indicate as there is Ag and O in the sample. Furthermore, the as synthesised sample of ZWO and ZW-10 and AZW-3 and calcined AAZW-3 show in the Figure 4.4(b2), 4.5b, 4.5d and 4.5f indicates the existance of Zn, Fe, O in the all mentioned samples and additianally Ag in the $Ag_2O/ZnFe_2O_4$(AZW-3) and calcined $Ag_2O/ZnFe_2O_4$(AAZW-3) composites.

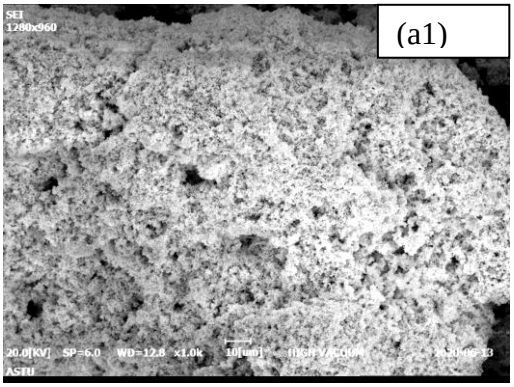

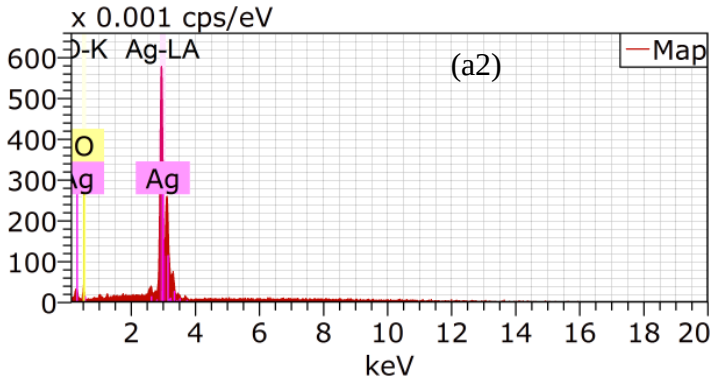

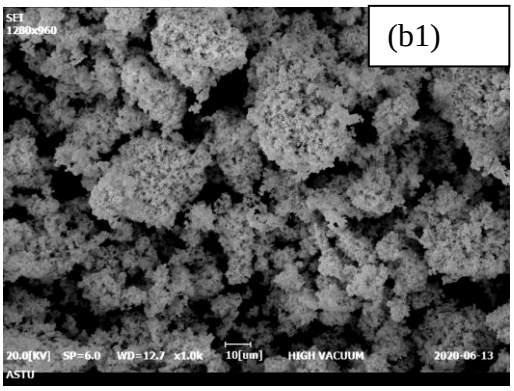

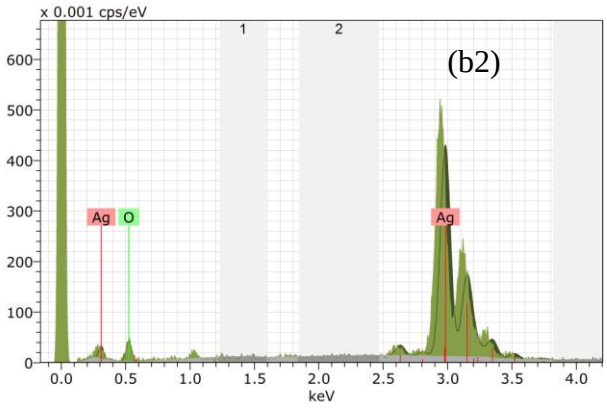

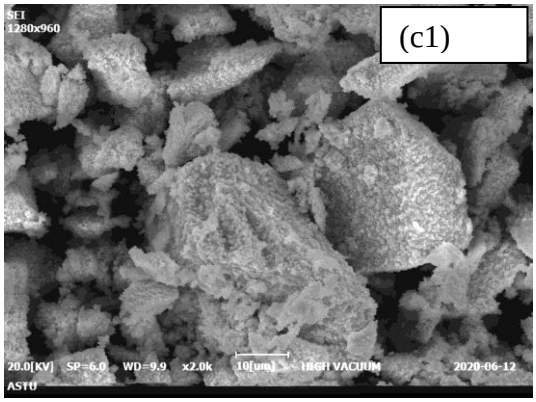

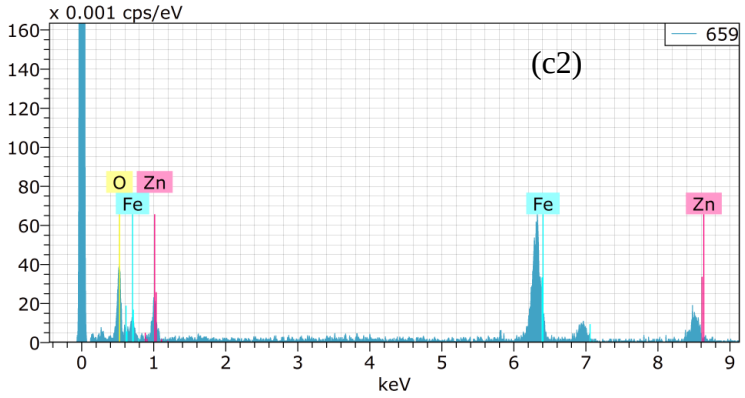

Figure 4.4 (a1), (b1) and (c1) show SEM image of A, ZWO and AA respectively. (a2), (b2) and (c2) show EDS mapping of A, ZWO and AA respectively.

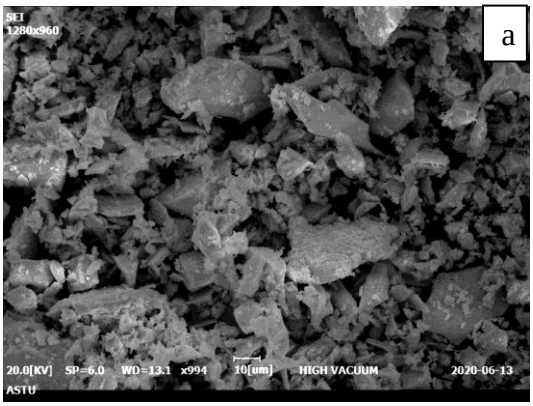

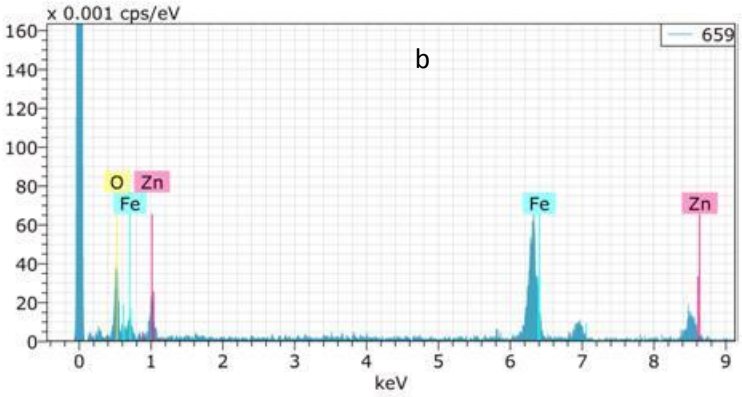

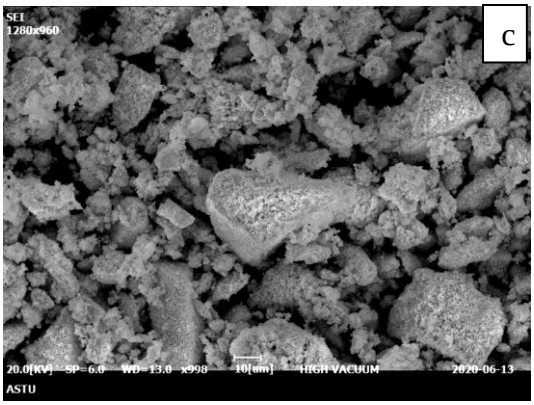

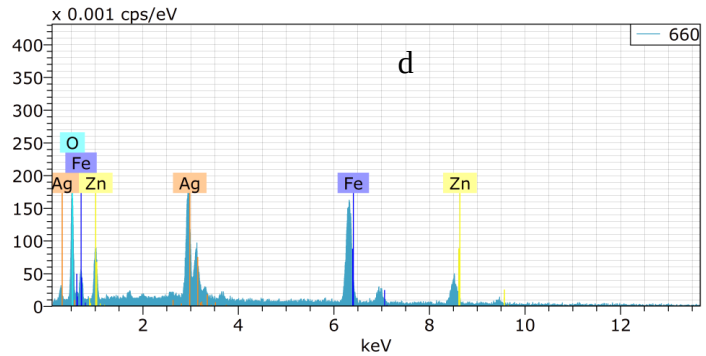

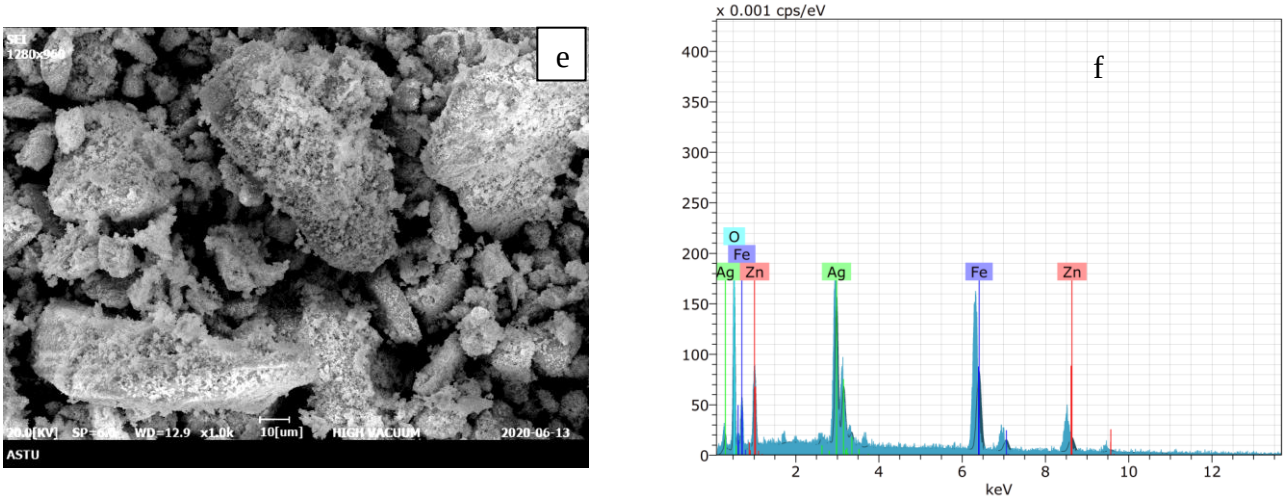

Figure 4.5 a, c and e shows SEM image ZW-10, AZW-3 and AAZW-3 respectively. b, d and f show EDS mapping of ZW-10, AZW-3 and AAZW-3 respectively.

4.5. Photocatalytic activity evaluation

Here in, the photocatalytic activities of all as synthesized samples were evaluated by the degradation of methylene blue dye using a visible light irradiation. The methylene blue dye has absorption peak shown at 664 nm in UV-visible-spectrometer [137]. As a reference, methylene blue dye without addition of any catalyst was exposed to visible light and the degradation was evaluated. As shown in the Figure 4.6a, and b, the degradation efficiency of methylene blue dye without catalyst was insignificant even after 80 min of light radiation. All the synthesized samples showed a significance degradation performance on the methylene blue dye as presented in Figure 4.6a and b. Moreover, the photocatalytic activity of ZW-10 shows higher efficiency of about 54% after 80 min light radiation with the corresponding reaction rate order, *k*, of about 0.01283 min^{-1} than the ZWO sample, which was about 51% with corresponding *k* of about 0.01185 min^{-1}, which could be due to the surface morphology and nature of crystallite obtained from the green synthesis route [114]. Furthermore, (*x*)Ag_2O/ (1-*x*)$ZnFe_2O_4$ (x= 0.05, 0.1, 0.15 and 0.2) composites degrade MB dye efficiently under the visible light, because of the formation of a p-n junction at the interface of Ag_2O-$ZnFe_2O_4$. Among the different compositions of the $Ag_2O/ZnFe_2O_4$, the AZW-3 composite sample showed the highest degradation efficiency of about 65% with corresponding *k* of about 0.01362 min^{-1}. This is related to the decrease in the recombination rate of $ZnFe_2O_4$ as a result of the p-n junction formation between Ag_2O and $ZnFe_2O_4$ that facilitate electron hole seperation by forming built-in electric field between the junction [22]. When, the Ag_2O percent

increases, the degradation capacity of the synthesized $Ag_2O/ZnFe_2O_4$ composite also increase as shown in the Figure 4.6b. Further loading shields the active site on the surface of $ZnFe_2O_4$ and decrease the degredation efficieny due the excessive amount of the loaded Ag_2O that covers the space of the active site [22]. The degradation efficiency of $Ag_2O/ZnFe_2O_4$ composite is still not adequate due to the challenges of the charge carrier recombinations. To further enhance the degradation efficiency, Ag was introduced into the compsoites of $(x)Ag_2O/(1-x)ZnFe_2O_4$ by decomposition of Ag_2O through calcination process. Among the calcined samples, $Ag_2O/ZnFe_2O_4$ composites with AAZW-3 showed the highest photocatalytic degradation efficency of about 90% within a degradation time of 80 min (k = 0.039 min^{-1}) due to the local surface plasmonic effect of Ag. This means that fast transfer of electrons from Ag can further elongate the recombination time of electrons and holes [77] so that the overall degradation perfromance can be enhanced. Further loading of Ag/Ag_2O on $ZnFe_2O_4$ leads to the deterioration of the degradation efficiency of the composite due to the active site shielded because of maximum loading [42]. All of the as-synthesized samples show pseudo first order reaction kinetics as the shown in Figure 4.6d. The kinetic equation is given as follows using equation [42]:

$$\ln(c_t/c_o) = -kt_{min}$$

where C_t is the concentration of the MB absorbed aftet time t in minute, C_o is initial concentration of the dye , k is reaction rate constant of the reaction and t_{min} is the time at which the absorbance of the dye measure. Additionally, the reaction rate (k) and correlation factor (R^2) [133] value of the as synthesized samples are shown and summarized in Table 7 indicates as the assynthesized sample undergo first order reaction.

Table 7 The value of *k* and R^2 of as synthesized samples.

Sample code	***k* (min^{-1})**	**R^2**
Blank	0.0028	0.9864
ZWO	0.0118	0.87228
ZW-9	0.01078	0.96235
ZW-10	0.01283	0.97587
ZW-11	0.01078	0.96235
A	0.01651	0.81288
AA	0.02345	0.87566
AZW-1	0.00859	0.9405
AZW-2	0.01223	0.8821
AZW-3	0.01362	0.9495
AZW-4	0.0114	0.8827
AAZW-1	0.01179	0.8818
AAZW-2	0.01423	0.8899
AAZW-3	0.039	0.8749
AAZW-4	0.01253	0.9162
AAZW-3-1	0.0253	0.9661
AAZW-3-2	0.02232	0.9487

Further more, the photocatalytic efficiency of Ag_2O (A) and Ag/Ag_2O (AA) was evaluated and the result indicates that A has low degreadation eficiency (69.15%) with *k* value of about 0.01078 min^{-1} when compared to AA that has a degradation efficiency 77.67% with *k* value of 0.01651 min^{-1}, as shown in the Figure 4.6a and 4.6b. This indicates that the incorporation of Ag enhance the photocatalytisc efficiency of Ag_2O by elongating the charge carrier recombination time Ag_2O and increase the number of charge carriers participating in the degradation process due to the high light absorption capacity of Ag [111]. The effect of calcination temperature on the synthesis of the Ag, which further affects the degradation capacity of calcined $Ag_2O/ZnFe_2O_4$ composite is also shown in the Figure 4.6a and 4.6b. The assythesized sample, which was calcined at 280 ºC (AAZW-3) showed high degradation efficiency of about 90% with the *k* value of 0.039 min^{-1} due to the adeaquate formation of Ag. Moreover, the calcination temperature is probably high enough

to promote the formationof chemical bonds between Ag, Ag_2O and $ZnFe_2O_4$ that results in smooth charge transfer to the surface [27, 42]. However, the degradation efficiency of the $Ag_2O/ZnFe_2O_4$ composite calcined at 300 ºC and 260 ºC was lower than that of the 280 ºC, this may correspond to maximum and insufficieny amount of Ag loaded on $Ag_2O/ZnFe_2O_4$ composite, respectively. Moreover, maximum calcination temperature lead to the agglomeration of Ag particle and active site shielding further lead to the deteoriation of the degradation efficiency as presented in this work AAZW-3-2 has low degradation efficiency (77.72%) than that of AAZW-3 (90%) after 80 min light irradiation [138].

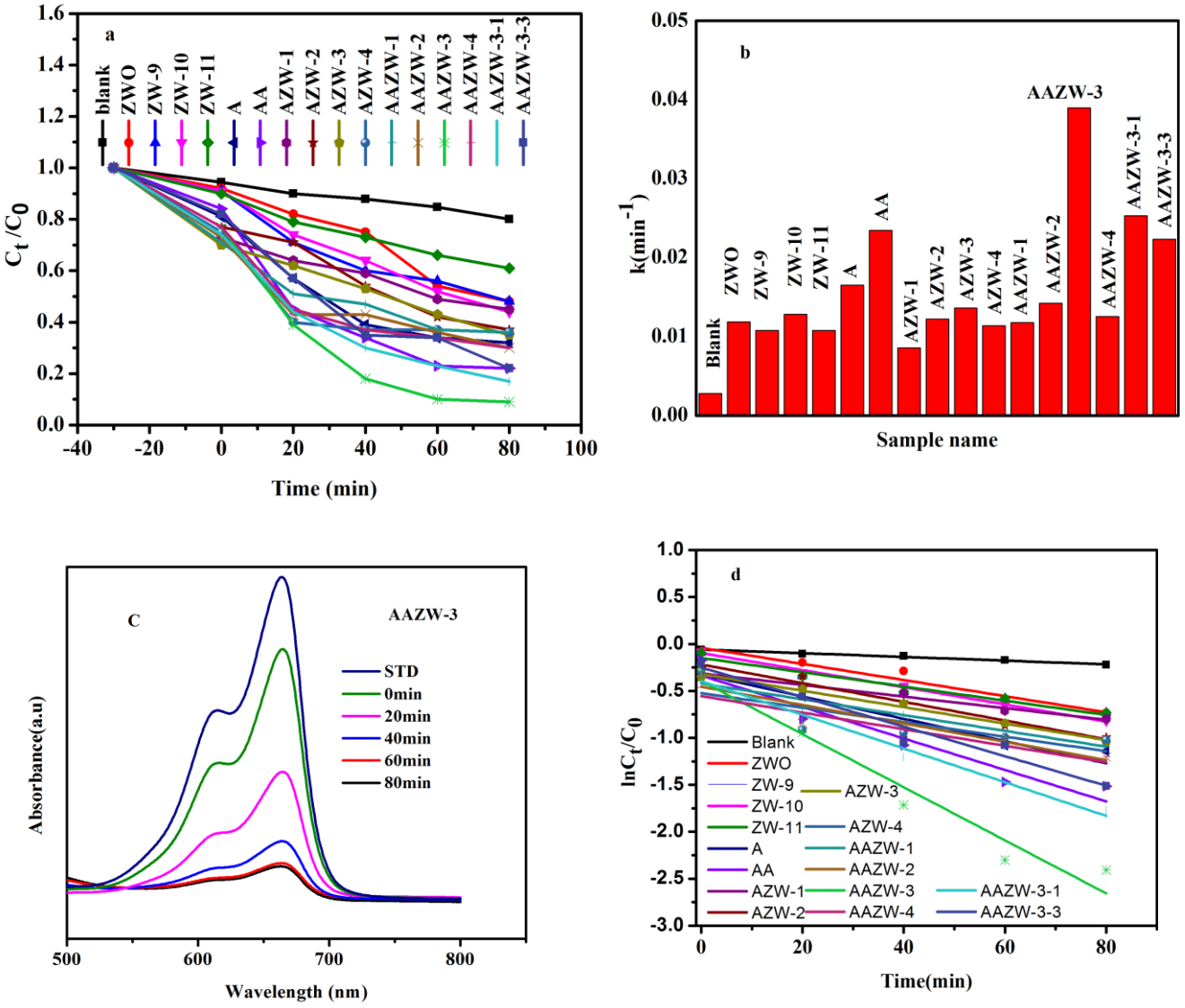

Figure 4.6 Photocatalytic activity as synthesized samples a. Reaction rate of as synthesized

sample b. Absorbance versus wavelength graph of AAZW-3 c. Kinetic for degradation of methylene blue for the as synthesized samples d.

4.6. Reusability test and pH effect analysis

To determine the stability of the AAZW-3 composite reusability experiment was carried out on the degradation of methylene blue. As shown in the Figure 4.7(a), the composite showed a slight decrease in the degradation efficiency for the first three cycles, while after fourth cycle the efficiency of the catalyst reduced very rapidly. The reduction of the efficiency of the catalyst deteroirate due to the photocorrosion effect of the catalyst [22].

Furthermore, the effect of pH on the photocatalytic efficiency of the samples was studied by varying the pH of the solution, which is due to the fact that the effleunts and wastewater discharged from the industries could be at different pH values [31]. The experiment conducted for the degradation of the MB in acidic media was at a pH of 4, while the basic media was at a pH of 10. Moreover, the degradation of the dye at neutral (pH =7) condition was carried out to evaluate the performance of the catalyst in neutral region. As shown in the Figure 4.7(b), degradation efficiency of the AAZW-3 is higher in basic media due to the fact that the surface of the catalyst $ZnFe_2O_4$ is negatively charged and oppositely charged MB adsorption to the surface of the catalyst can be enhanced as a result of interatomic attraction force [54]. However, the degradation efficiency of the AAZW-3 decreased in acidic media, which could be related to the positively charged surface of the catalyst and the MB dye, which have the same charge could results in the repulsion effect and therefore the adsorption capacity of the cataltyst is minimal [54]. Moreover, the photocatalytic activity of the AAZW-3 is satisfactory in the neutral region as a result of the surface of the $ZnFe_2O_4$ is negatively charge that leads to the attraction of the cationic dye to the surface [54] and therefore leads to the degradation effect of the MB.

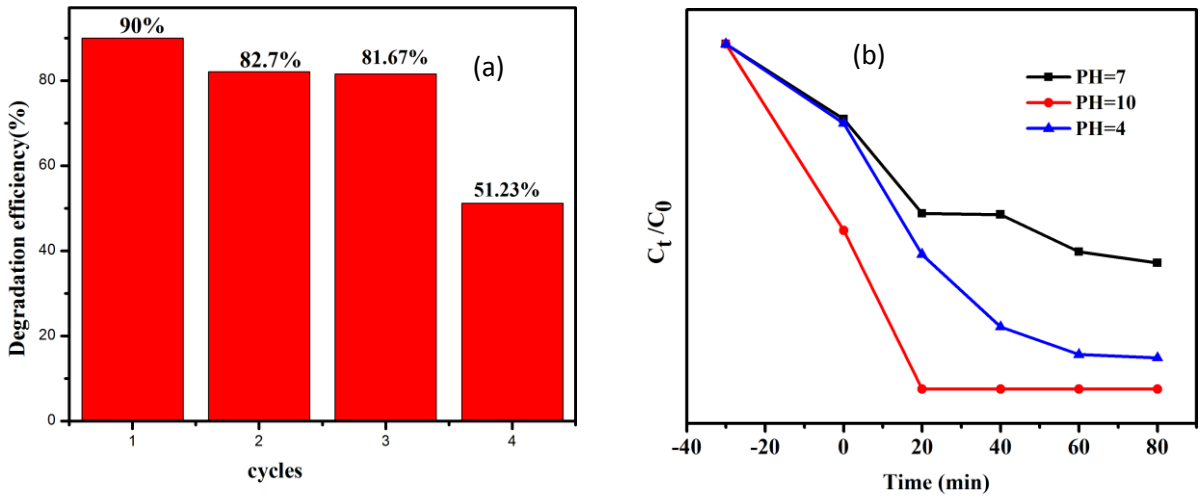

Figure 4.7 Reusability and pH dependence MB degradation. (a) Cyclic degradation of MB on AAZW-3, (b) degradation of MB in different pH conditions using AAZW-3,

4.7. Proposed degradation Mechanism

Based on the previously reported literature works [27], the reaction mechanism of the AAZW-3 was indicated in the Figure 4.8 below.

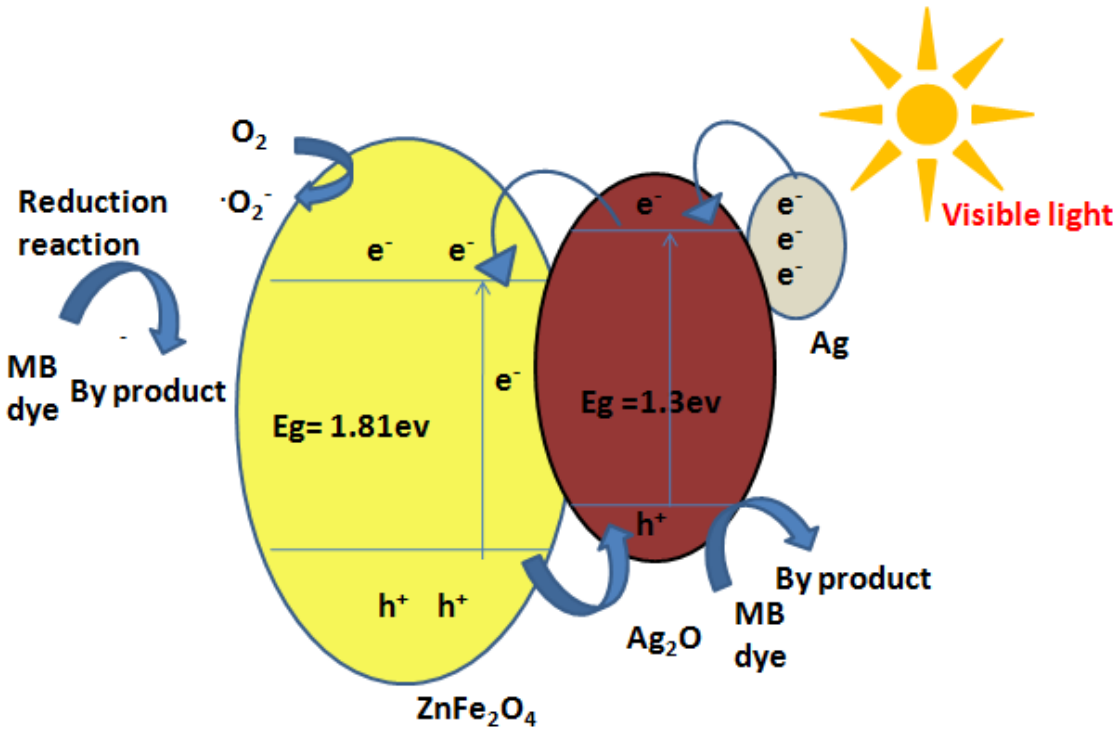

Figure 4.8 Proposed degradation mechanism of AAZW-3 composite

During light irradiation both the $ZnFe_2O_4$ and Ag_2O response to the visible light [27] due to their band gap (E_g). Moreover, the electron formed on the surface of Ag as a result of the plasmonic effect during the light radiation move to the conduction band of the Ag_2O [27]. The movement of the electron from Ag to the Ag_2O is due to the difference in the work function between Ag (3.54 eV/AVS) and Ag_2O (3.67 eV/AVS) [111]. The electron accumulated in conduction band of the Ag_2O (conduction band edge = -0.14eV/NHE) moves to the conduction band of $ZnFe_2O_4$ (conduction band edge = -0.98 eV/NHE) due to the difference in the conduction band level [22]. Moreover, there is a formation of superoxide radical ($\bullet O_2^-$) due to the reaction between the absorbed oxygen (O_2) and the electron accumulated in the surface of $ZnFe_2O_4$ as a result of the electrons in the conduction band of $ZnFe_2O_4$ negative enough (-0.98 eV/NHE) to reduce absorbed O_2 (reduction potential O_2 = -0.046 eV/NHE) [22]. The formed superoxide radical and electrons participate in the degradation of the MB dye [22, 42]. However, the holes in the valence band of Ag_2O hardly satisfied the requirement of hydroxyl radicals (•OH) generation ($H_2O/^{\bullet}OH^-$, +2.4eV) instead (•OH) formed from the intermediate reaction a shown on the equation [23, 137]. Here in, the holes and hydroxyl radical may participate in the degradation process as indicated in the following equations. Finally, intermediate compounds, H_2O and CO_2 formed from the reaction [137].

$$Ag/Ag_2O/ZnFe_2O_4 + \boldsymbol{h\nu} \longrightarrow Ag_2O\,(e^-, h^+) + Ag\,(e^-) + ZnFe_2O_4\,(e^-, h^+) \quad \ldots\ldots(1)$$

$$h^+\,(ZnFe_2O_4) + Ag_2O \longrightarrow Ag_2O\,(h^+) \quad \ldots\ldots(2)$$

$$Ag_2O + e^-(Ag) \longrightarrow Ag_2O\,(e^-) \quad \ldots\ldots(3)$$

$$Ag_2O\,(e^-) + ZnFe_2O_4 \longrightarrow ZnFe_2O_4\,(e^-) \quad \ldots\ldots(4)$$

$$e^- + O_2 \longrightarrow {}^{\bullet}O_2^- \quad \ldots\ldots(5)$$

$${}^{\bullet}O_2^- + H_2O \longrightarrow \bullet HO_2 + OH^- \quad \ldots\ldots(6)$$

$${}^{\bullet}HO_2 + H_2O \longrightarrow H_2O_2 + \bullet OH \quad \ldots\ldots(7)$$

$H_2O_2 \longrightarrow 2\bullet OH$……(8)

$^{\bullet}OH$ + MB dye ⟶ Dye degradation product……..…….....(9)

h^+ + MB dye ⟶ Dye degradation product….....(10)

In the above equations, ***h*** is the Plank constant ($6.625x10^{34}$ J·s), ***v*** is the light frequency (Hz), the product between the two (***hv***) is the energy of the light (***E***). The holes are representing by (h^+), while electrons are represented by (e^-) and other parameters are defined.

CHAPTER FIVE

5. Conclusions and Recommendations

5.1. Conclusions

In this work, green synthesis route was successfully used to synthesize $ZnFe_2O_4$ by utilizing *Ajuga integrafolia* plant as a capping/stabilizing agent. The TGA-DTA experiment was carried out to find the temperature at which $ZnFe_2O_4$ starts to form and the result revealed that the formation temperature is above 400 °C. Single phase of $ZnFe_2O_4$ was obtained after calcination at a temperature of 1000 °C, designated as ZW-10, as confirmed by using X-ray diffraction experiment.

A composites of Ag_2O and ZW-10 with the composition of (x) Ag_2O/(1-x) $ZnFe_2O_4$ (x = 0.05, 0.01, 0.15 and 0.2) composite was synthesized by facile deposition precipitation technique. The decomposition of Ag_2O to Ag by calcination at a temperature of 280 °C introduced plasmonic effect into the composites of $Ag_2O/ZnFe_2O_4$, which enhanced the degradation efficiency of the composite, with an optimum of 15%Ag_2O/85% $ZnFe_2O_4$. Moreover, the effect of calcination temperature on the optimized binary composite of 15% Ag_2O/85% $ZnFe_2O_4$ carried out by varying the calcination temperature from 260, 280 and 300 °C. Though the sample calcined at 300 °C showed high quantity of Ag formation (as confirmed from XRD pattern), the sample calcined at 280 °C showed an optimum degradation performance. This is because the former sample suffers from the agglomeration of Ag on the surface of the composite.

The photocatalytic performance of the as synthesized samples towards the degradation of MB dye under visible light radiation was performed and the UV-visible spectrometer was utilized to measure the absorbance of MB dye around the wavelength of 664 nm. All the as-synthesized samples significantly degrade MB dye under the radiation of visible light. A sample of $ZnFe_2O_4$ synthesized with plan extract and calcined at 1000 °C, i.e., ZW-10 showed a degradation percentage of about 54%, which is higher than that of the $ZnFe_2O_4$ synthesized without plant, ZWO, which had a degradation efficiency of about 51%, mainly attributed to the crystallinity and surface morphology of the samples. Moreover, the loading of Ag_2O on $ZnFe_2O_4$ increased the photocatalytic degradation efficiency due to the formation of a p-n junction at the interface of

Ag_2O and $ZnFe_2O_4$, as they are *p*- and *n*-type oxide materials, respectively. Among these composites, the sample with a composition of 15%Ag_2O/85% $ZnFe_2O_4$ or designated as AZW-3 showed an optimum degradation performance with a corresponding degradation efficiency of about 65%. Calcination also improved the degradation efficiency by incorporation of Ag into the composites and thereby forming $Ag/Ag_2O/ZnFe_2O_4$ (AAZW) composites. The sample with a composition of 15%(Ag/Ag_2O)/85%$ZnFe_2O_4$(AAZW-3) showed the optimum degradation efficiency of about 90% within 80 min of degradation time due to the local surface plasmonic effect of Ag. Additionally, AAZW-3 photocatalytic recoverability and performance was performed up to three cycles without significant decrease in efficiency. However, after the fourth cycle, the degradation efficiency deteriorates due to photocorrosion effect. Moreover, AAZW-3 composite showed highest photocatalytic efficiency in the basic media because of strong interaction between the catalyst surface and the MB dye, which further enhanced the adsorption and degradation of the MB dye.

Therefore, the materials developed in this work, i.e., 15% (Ag/Ag_2O)/85% $ZnFe_2O_4$ can be a potential candidate materials to efficiently degrade and remove the MB from any of the industrial effluents and wastewater before discharging into the environment.

5.2. Recommendations

Removal of unwanted and toxic substances from industrial effluents and wastewater is essential before their discharge to the environment to protect the environmental pollution and therefore secures societal wellbeing. In this work, we showed that the composites of $Ag_2O/ZnFe_2O_4$showed a promising degradation of MB dye so that it can be removed from the industrial effluents and wastewater. However, many works are still under progress and we recommend the following.

The present materials were investigated towards the removal of MB and the maximum degradation efficiency was only about 90%, which requires further optimization processes through nanostructuring approaches. These can be achieved by fine-tuning of the synthesis parameters and methodologies such as hydrothermal, solvothermal, chemical vapor deposition (CVD), physical vapor deposition (PVD) and perhaps sol-gel methods, which can in turn increases the surface morphologies of the composite materials and therefore the active surface area of the photocatalytic materials that leads to the high degradation efficiency of more than 95%. Moreover, we also

recommend the investigation of the materials towards other organic dyes, which are toxic, when released to the environment.

Furthermore, we recommend on the trapping experiment for identification of the active species, which can determine the active species and the degradation mechanism that was not performed in this thesis work due to the unavailability of the scavengers [111]. Photoluminescence (PL) spectroscopy and Mott-Schotkky analysis are also recommended for measuring the recombination rate and the flat band potential of semiconductors, respectively, where the latter technique confirms if the interface formed is a p-n or Schottky junction.

Our last, but not least recommendation is that, the surface morphology can be better understood if high-magnification electron microscopies such as transmission electron microscopies (TEM) can be utilized in order to visualize and further engineer the surface morphologies and particle size of the composite powder. Specific surface area (SSA) plays a very important role in this work and due to the unavailability of the Bruner-Emmitt-Teller (BET), we were not able to perform the determination of the SSA. Therefore, we further recommend the BET experiment on the present sample and the samples to be used for this type of applications.

APPENDIX

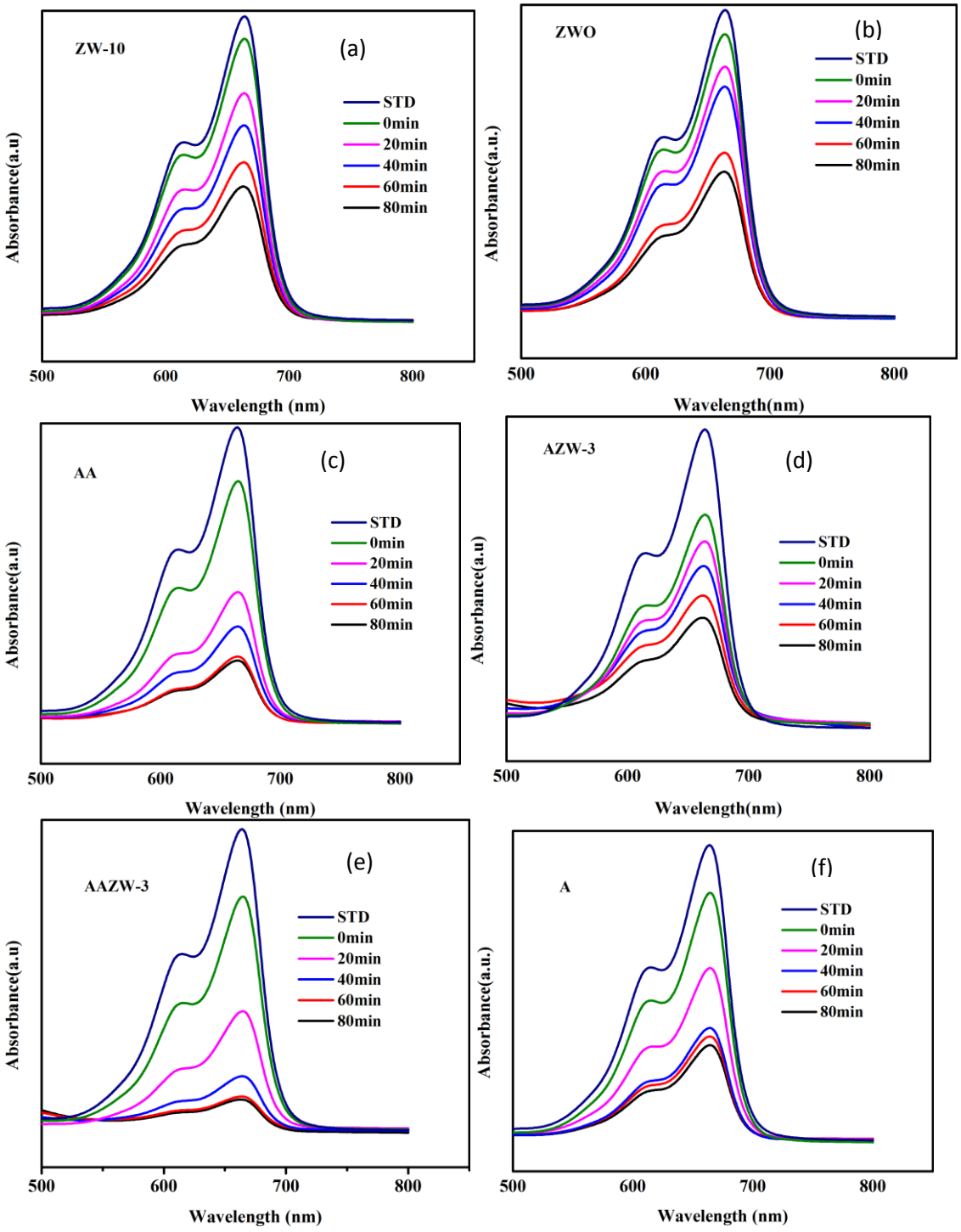
ZW-10
(a)
STD
0min
20min
40min
60min
80min
Absorbance(a.u)
Wavelength (nm)
ZWO
(b)
Absorbance(a.u.)
Wavelength(nm)
AA
(c)
AZW-3
(d)
AAZW-3
(e)
A
(f)
500
600
700
800

References

[1] S. Jalali, M.R. Rahimi, K. Dashtian, M. Ghaedi, S. Mosleh, One step integration of plasmonic Ag_2CrO_4/Ag/AgCl into HKUST-1-MOF as novel visible-light driven photocatalyst for highly efficient degradation of mixture dyes pollutants: Its photocatalytic mechanism and modeling, Polyhedron, 166 (2019) 217-225.

[2] P. Dai, M. Wu, T. Jiang, H. Hu, X. Yu, Z. Bai, Silver-loaded ZnO/$ZnFe_2O_4$ mesoporous hollow spheres with enhanced photocatalytic activity for 2,4-dichlorophenol degradation under visible light irradiation, Materials Research Bulletin, 107 (2018) 339-346.

[3] H.-W. David Kuo, I. Xagoraraki, Contaminants Associated with Drinking Water, in: S.R. Quah (Ed.) International Encyclopedia of Public Health (Second Edition), Academic Press, Oxford, 2017, pp. 148-158.

[4] L. Zou, Q. Wang, X. Shen, Z. Wang, M. Jing, Z. Luo, Fabrication and dye removal performance of magnetic $CuFe_2O_4$@CeO_2 nanofibers, Applied Surface Science, 332 (2015) 674-681.

[5] N. Güy, M. Özacar, Ag/Ag_2CrO_4 nanoparticles modified on ZnO nanorods as an efficient plasmonic photocatalyst under visible light, Journal of Photochemistry and Photobiology A: Chemistry, 370 (2019) 1-11.

[6] K. Kaur, R. Jindal, Synergistic effect of organic-inorganic hybrid nanocomposite ion exchanger on photocatalytic degradation of Rhodamine-B dye and heavy metal ion removal from industrial effluents, Journal of Environmental Chemical Engineering, 6 (2018) 7091-7101.

[7] G. Mamba, A. Mishra, Advances in Magnetically Separable Photocatalysts: Smart, Recyclable Materials for Water Pollution Mitigation, Catalysts, 6 (2016) 79.

[8] K.G. Pavithra, S.K. P, J. V, S.R. P, Removal of colorants from wastewater: A review on sources and treatment strategies, Journal of Industrial and Engineering Chemistry, 75 (2019) 1-19.

[9] O.M. Rodriguez-Narvaez, J.M. Peralta-Hernandez, A. Goonetilleke, E.R. Bandala, Treatment technologies for emerging contaminants in water: A review, Chemical Engineering Journal, 323 (2017) 361-380.

[10] C.L. Yang, J. McGarrahan, Electrochemical coagulation for textile effluent decolorization, Journal of hazardous materials, 127 (2005) 40-47.

[11] O. Adnan, Z.Z. Abidin, A. Idris, S. Kamarudin, M.S. Al-Qubaisi, A novel biocoagulant agent from mushroom chitosan as water and wastewater therapy, Environmental science and pollution research international, 24 (2017) 20104-20112.

[12] M. Bellardita, A. Di Paola, B. Megna, L. Palmisano, Determination of the crystallinity of TiO_2 photocatalysts, Journal of Photochemistry and Photobiology A: Chemistry, 367 (2018) 312-320.

[13] H. Li, Y. Li, C. Wang, J. Li, Z-scheme Ag_2O/Ag/amorphous TiO_2 shells for enhanced plasmonic photoelectrochemical assay of nitrogen dioxide, Sensors and Actuators B: Chemical, 289 (2019) 138-143.

[14] S. Ma, J. Xue, Y. Zhou, Z. Zhang, Photochemical synthesis of ZnO/Ag_2O heterostructures with enhanced ultraviolet and visible photocatalytic activity, J. Mater. Chem. A, 2 (2014) 7272-7280.

[15] H.-Y. Wu, W.-J. Jian, H.-F. Dang, X.-F. Zhao, L.-Z. Zhang, J.-H. Li, Hierarchical Ag-ZnO Microspheres with Enhanced Photocatalytic Degradation Activities, Polish Journal of Environmental Studies, 26 (2017) 871-880.

[16] Y. Guan, H.Y. Yu, S.Y.H. Abdalkarim, C. Wang, F. Tang, J. Marek, W.L. Chen, J. Militky, J.M. Yao, Green one-step synthesis of ZnO/cellulose nanocrystal hybrids with modulated morphologies and superfast absorption of cationic dyes, International journal of biological macromolecules, 132 (2019) 51-62.

[17] N. Zhang, D. Chu, Fabrication of flower-like hierarchical ZnO nanostructures with enhanced photocatalytic activity, Surfaces and Interfaces, 14 (2019) 251-255.

[18] K. Praveena, K. Sadhana, S. Bharadwaj, S.R. Murthy, Development of nanocrystalline Mn–Zn ferrites for high frequency transformer applications, Journal of Magnetism and Magnetic Materials, 321 (2009) 2433-2437.

[19] S.F. Medeiros, A.M. Santos, H. Fessi, A. Elaissari, Stimuli-responsive magnetic particles for biomedical applications, International Journal of Pharmaceutics, 403 (2011) 139-161.

[20] K. Niemirowicz, K.H. Markiewicz, A.Z. Wilczewska, H. Car, Magnetic nanoparticles as new diagnostic tools in medicine, Advances in Medical Sciences, 57 (2012) 196-207.

[21] Y. Cao, X. Lei, Q. Chen, C. Kang, W. Li, B. Liu, Enhanced photocatalytic degradation of tetracycline hydrochloride by novel porous hollow cube $ZnFe_2O_4$, Journal of Photochemistry and Photobiology A: Chemistry, 364 (2018) 794-800.

[22] H. Guo, H.-Y. Niu, C. Liang, C.-G. Niu, D.-W. Huang, L. Zhang, N. Tang, Y. Yang, C.-Y. Feng, G.-M. Zeng, Insight into the energy band alignment of magnetically separable $Ag_2O/ZnFe_2O_4$ p-n heterostructure with rapid charge transfer assisted visible light photocatalysis, Journal of Catalysis, 370 (2019) 289-303.

[23] Y. Sun, C. Shao, X. Li, X. Guo, X. Zhou, X. Li, Y. Liu, Hierarchical heterostructures of p-type bismuth oxychloride nanosheets on n-type zinc ferrite electrospun nanofibers with enhanced visible-light photocatalytic activities and magnetic separation properties, Journal of colloid and interface science, 516 (2018) 110-120.

[24] Y. Xu, Q. Liu, M. Xie, S. Huang, M. He, L. Huang, H. Xu, H. Li, Synthesis of zinc ferrite/silver iodide composite with enhanced photocatalytic antibacterial and pollutant degradation ability, Journal of colloid and interface science, 528 (2018) 70-81.

[25] F. Sun, Q. Zeng, W. Tian, Y. Zhu, W. Jiang, Magnetic MFe_2O_4-Ag_2O (M = Zn, Co, & Ni) composite photocatalysts and their application for dye wastewater treatment, Journal of Environmental Chemical Engineering, 7 (2019) 103011.

[26] Y. Huang, D. Zhu, Q. Zhang, Y. Zhang, J.-j. Cao, Z. Shen, W. Ho, S.C. Lee, Synthesis of a $Bi_2O_2CO_3/ZnFe_2O_4$ heterojunction with enhanced photocatalytic activity for visible light irradiation-induced NO removal, Applied Catalysis B: Environmental, 234 (2018) 70-78.

[27] X. Li, D. Tang, F. Tang, Y. Zhu, C. He, M. Liu, C. Lin, Y. Liu, Preparation, characterization and photocatalytic activity of visible-light-driven plasmonic $Ag/AgBr/ZnFe_2O_4$ nanocomposites, Materials Research Bulletin, 56 (2014) 125-133.

[28] A.R. Upreti, Y. Li, N. Khadgi, S. Naraginti, C. Zhang, Efficient visible light photocatalytic degradation of 17α-ethinyl estradiol by a multifunctional $Ag–AgCl/ZnFe_2O_4$ magnetic nanocomposite, RSC Advances, 6 (2016) 32761-32769.

[29] J. Xie, Q. Wu, D. Zhao, Electrospinning synthesis of $ZnFe_2O_4/Fe_3O_4$/Ag nanoparticle-loaded mesoporous carbon fibers with magnetic and photocatalytic properties, Carbon, 50 (2012) 800-807.

[30] I.Y. López-Pacheco, A. Silva-Núñez, C. Salinas-Salazar, A. Arévalo-Gallegos, L.A. Lizarazo-Holguin, D. Barceló, H.M.N. Iqbal, R. Parra-Saldívar, Anthropogenic contaminants of high concern: Existence in water resources and their adverse effects, Science of The Total Environment, 690 (2019) 1068-1088.

[31] S. Nahar, M.R. Hasan, A.A.H. Kadhum, H.A. Hasan, M.F.M. Zain, Photocatalytic degradation of organic pollutants over visible light active plasmonic Ag nanoparticle loaded

Ag_2SO_3 photocatalysts, Journal of Photochemistry and Photobiology A: Chemistry, 375 (2019) 191-200.
[32] M. Hao, T. Yi, Y. Cao, Y. Song, Z. Cao, W. He, Y. Gao, J. Liu, Enhanced visible light photocatalytic activity in AgI/BiOCOOH composite, Advanced Powder Technology, 30 (2019) 111-119.
[33] S.S. Moghaddam, M.R. Moghaddam, M. Arami, Coagulation/flocculation process for dye removal using sludge from water treatment plant: optimization through response surface methodology, Journal of hazardous materials, 175 (2010) 651-657.
[34] M.H. Zhang, H. Dong, L. Zhao, D.X. Wang, D. Meng, A review on Fenton process for organic wastewater treatment based on optimization perspective, The Science of the total environment, 670 (2019) 110-121.
[35] R. Andreozzi, M. Canterino, R. Marotta, Fe(III) homogeneous photocatalysis for the removal of 1,2-dichlorobenzene in aqueous solution by means UV lamp and solar light, Water research, 40 (2006) 3785-3792.
[36] M. Pelaez, N.T. Nolan, S.C. Pillai, M.K. Seery, P. Falaras, A.G. Kontos, P.S.M. Dunlop, J.W.J. Hamilton, J.A. Byrne, K. O'Shea, M.H. Entezari, D.D. Dionysiou, A review on the visible light active titanium dioxide photocatalysts for environmental applications, Applied Catalysis B: Environmental, 125 (2012) 331-349.
[37] A. Singh, D.P. Dutta, A. Ballal, A.K. Tyagi, M.H. Fulekar, Visible light driven photocatalysis and antibacterial activity of $AgVO_3$ and $Ag/AgVO_3$ nanowires, Materials Research Bulletin, 51 (2014) 447-454.
[38] P. Tun, K. Wang, H. Naing, J. Wang, G. Zhang, Facile preparation of visible-light-responsive kaolin-supported Ag@AgBr composites and their enhanced photocatalytic properties, Applied Clay Science, 175 (2019) 76-85.
[39] J.-F. Guo, B. Ma, A. Yin, K. Fan, W.-L. Dai, Photodegradation of rhodamine B and 4-chlorophenol using plasmonic photocatalyst of $Ag–AgI/Fe_3O_4@SiO_2$ magnetic nanoparticle under visible light irradiation, Applied Catalysis B: Environmental, 101 (2011) 580-586.
[40] R. Liu, P. Wang, X. Wang, H. Yu, J. Yu, UV- and Visible-Light Photocatalytic Activity of Simultaneously Deposited and Doped $Ag/Ag(I)-TiO_2$ Photocatalyst, The Journal of Physical Chemistry C, 116 (2012) 17721-17728.
[41] X. Chen, Y. Dai, J. Guo, T. Liu, X. Wang, Novel Magnetically Separable Reduced Graphene Oxide (RGO)/$ZnFe_2O_4$/Ag_3PO_4 Nanocomposites for Enhanced Photocatalytic Performance toward

2,4-Dichlorophenol under Visible Light, Industrial & Engineering Chemistry Research, 55 (2016) 568-578.

[42] H. Guo, C.-G. Niu, D.-W. Huang, N. Tang, C. Liang, L. Zhang, X.-J. Wen, Y. Yang, W.-J. Wang, G.-M. Zeng, Integrating the plasmonic effect and p-n heterojunction into a novel $Ag/Ag_2O/PbBiO_2Br$ photocatalyst: Broadened light absorption and accelerated charge separation co-mediated highly efficient visible/NIR light photocatalysis, Chemical Engineering Journal, 360 (2019) 349-363.

[43] W. Lv, B. Wei, L. Xu, Y. Zhao, H. Gao, J. Liu, Photocatalytic properties of hierarchical ZnO flowers synthesized by a sucrose-assisted hydrothermal method, Applied Surface Science, 259 (2012) 557-561.

[44] N. Rosman, W.N.W. Salleh, A.F. Ismail, J. Jaafar, Z. Harun, F. Aziz, M.A. Mohamed, B. Ohtani, M. Takashima, Photocatalytic degradation of phenol over visible light active $ZnO/Ag_2CO_3/Ag_2O$ nanocomposites heterojunction, Journal of Photochemistry and Photobiology A: Chemistry, 364 (2018) 602-612.

[45] D. Zhang, F. Dai, P. Zhang, Z. An, Y. Zhao, L. Chen, The photodegradation of methylene blue in water with PVDF/GO/ZnO composite membrane, Materials science & engineering. C, Materials for biological applications, 96 (2019) 684-692.

[46] S.W. Cao, Y.J. Zhu, G.F. Cheng, Y.H. Huang, $ZnFe_2O_4$ nanoparticles: microwave-hydrothermal ionic liquid synthesis and photocatalytic property over phenol, Journal of hazardous materials, 171 (2009) 431-435.

[47] Y. Wang, L. Liu, L. Xu, X. Cao, X. Li, Y. Huang, C. Meng, Z. Wang, W. Zhu, $Ag_2O/TiO_2/V_2O_5$ one-dimensional nanoheterostructures for superior solar light photocatalytic activity, Nanoscale, 6 (2014) 6790-6797.

[48] X. Wang, S. Li, H. Yu, J. Yu, S. Liu, Ag_2O as a new visible-light photocatalyst: self-stability and high photocatalytic activity, Chemistry, 17 (2011) 7777-7780.

[49] J. Zhang, Z. Ma, $Ag\text{-}Ag_3VO_4/AgIO_3$ composites with enhanced visible-light-driven catalytic activity, Journal of colloid and interface science, 524 (2018) 16-24.

[50] M. Pirhashemi, A. Habibi-Yangjeh, Ternary $ZnO/AgBr/Ag_2CrO_4$ nanocomposites with tandem n–n heterojunctions as novel visible-light-driven photocatalysts with excellent activity, Ceramics International, 41 (2015) 14383-14393.

[51] N.G. Yadav, L.S. Chaudhary, P.A. Sakhare, T.D. Dongale, P.S. Patil, A.D. Sheikh, Impact of collected sunlight on $ZnFe_2O_4$ nanoparticles for photocatalytic application, Journal of colloid and interface science, 527 (2018) 289-297.

[52] E. Prabakaran, K. Pillay, Synthesis of N-doped ZnO nanoparticles with cabbage morphology as a catalyst for the efficient photocatalytic degradation of methylene blue under UV and visible light, RSC Advances, 9 (2019) 7509-7535.

[53] R. Lamba, A. Umar, S.K. Mehta, S.K. Kansal, Enhanced visible light driven photocatalytic application of Ag_2O decorated ZnO nanorods heterostructures, Separation and Purification Technology, 183 (2017) 341-349.

[54] M. Malakootian, A. Nasiri, A. Asadipour, E. Kargar, Facile and green synthesis of $ZnFe_2O_4$@CMC as a new magnetic nanophotocatalyst for ciprofloxacin degradation from aqueous media, Process Safety and Environmental Protection, 129 (2019) 138-151.

[55] K.M. Reza, A. Kurny, F. Gulshan, Parameters affecting the photocatalytic degradation of dyes using TiO_2: a review, Applied Water Science, 7 (2017) 1569-1578.

[56] S.P. Pattnaik, A. Behera, S. Martha, R. Acharya, K. Parida, Synthesis, photoelectrochemical properties and solar light-induced photocatalytic activity of bismuth ferrite nanoparticles, Journal of Nanoparticle Research, 20 (2018).

[57] S. Babic, D. Ljubas, D.I. Sipusic, L. Curkovic, J. Beganovic, Effects of pH and water matrix on photoinduced degradation of antibiotic cefdinir, proceedings of the 4th world congress on civil, structural and Environmental Engineering ICEPTP 118 (2019) 1-12.

[58] K.S. Kumar, V. Samynaathan, S. Kumar, B. Neeraja, Photocatalytic degradation of methylene blue dye using dysprosium oxide/bismuth oxide nanocomposite, Journal of Environmental Biology, 40 (2019) 825-831.

[59] J. Ahmad, K. Majid, M.A. Dar, Controlled synthesis of p-type NiO/n-type GO nanocomposite with enhanced photocatalytic activity and study of temperature effect on the photocatalytic activity of the nanocomposite, Applied Surface Science, 457 (2018) 417-426.

[60] F. Meng, Y. Liu, J. Wang, X. Tan, H. Sun, S. Liu, S. Wang, Temperature dependent photocatalysis of g-C_3N_4, TiO_2 and ZnO: Differences in photoactive mechanism, Journal of colloid and interface science, 532 (2018) 321-330.

[61] A. Salama, A. Mohamed, N.M. Aboamera, T.A. Osman, A. Khattab, Photocatalytic degradation of organic dyes using composite nanofibers under UV irradiation, Applied Nanoscience, 8 (2018) 155-161.

[62] Y. Xin, Q. Chen, G. Zhang, Construction of ternary heterojunction CuS-CdS/TiO_2 nanobelts for photocatalytic degradation of gaseous toluene, Journal of Alloys and Compounds, 751 (2018) 231-240.

[63] G. Han, L. Wang, C. Pei, R. Shi, B. Liu, H. Zhao, H. Yang, S. Liu, Size-dependent optical properties and enhanced visible light photocatalytic activity of wurtzite CdSe hexagonal nanoflakes with dominant {0 0 1} facets, Journal of Alloys and Compounds, 610 (2014) 62-68.

[64] R. Saravanan, V.K. Gupta, V. Narayanan, A. Stephen, Comparative study on photocatalytic activity of ZnO prepared by different methods, Journal of Molecular Liquids, 181 (2013) 133-141.

[65] G. Cernuto, N. Masciocchi, A. Cervellino, G.M. Colonna, A. Guagliardi, Size and Shape Dependence of the Photocatalytic Activity of TiO_2 Nanocrystals: A Total Scattering Debye Function Study, Journal of the American Chemical Society, 133 (2011) 3114-3119.

[66] M.M. Khan, S.F. Adil, A. Al-Mayouf, Metal oxides as photocatalysts, Elsevier, 2015.

[67] D. Papoulis, K. Somalakidi, N. Todorova, C. Trapalis, D. Panagiotaras, D. Sygkridou, E. Stathatos, E. Gianni, A. Mavrikos, S. Komarneni, Sepiolite/TiO_2 and metal ion modified sepiolite/TiO_2 nanocomposites: synthesis, characterization and photocatalytic activity in abatement of NO_x gases, Applied Clay Science, 179 (2019) 105-156.

[68] M. Irfan, M. Sevim, Y. Koçak, M. Balci, Ö. Metin, E. Ozensoy, Enhanced photocatalytic NO_x oxidation and storage under visible-light irradiation by anchoring Fe_3O_4 nanoparticles on mesoporous graphitic carbon nitride (mpg-C_3N_4), Applied Catalysis B: Environmental, 249 (2019) 126-137.

[69] A. Hanini, K. Kacem, J. Gavard, H. Abdelmelek, S. Ammar, Ferrite Nanoparticles for Cancer Hyperthermia Therapy, (2018) 638-661.

[70] D. Ma, J.-W. Shi, D. Sun, Y. Zou, L. Cheng, C. He, H. Wang, C. Niu, L. Wang, Au decorated hollow ZnO@ZnS heterostructure for enhanced photocatalytic hydrogen evolution: The insight into the roles of hollow channel and Au nanoparticles, Applied Catalysis B: Environmental, 244 (2019) 748-757.

[71] S.R. Kelly, X. Shi, S. Back, L. Vallez, S.Y. Park, S. Siahrostami, X. Zheng, J.K. Nørskov, ZnO as an Active and Selective Catalyst for Electrochemical Water Oxidation to Hydrogen Peroxide, ACS Catalysis, 9 (2019) 4593-4599.

[72] B.L. Martínez-Vargas, M. Cruz-Ramírez, J.A. Díaz-Real, J.L. Rodríguez-López, F.J. Bacame-Valenzuela, R. Ortega-Borges, Y. Reyes-Vidal, L. Ortiz- Frade, Synthesis and

characterization of n-ZnO/p-MnO nanocomposites for the photocatalytic degradation of anthracene, Journal of Photochemistry and Photobiology A: Chemistry, 369 (2019) 85-96.

[73] A. Serrà, Y. Zhang, B. Sepúlveda, E. Gómez, J. Nogués, J. Michler, L. Philippe, Highly active ZnO-based biomimetic fern-like microleaves for photocatalytic water decontamination using sunlight, Applied Catalysis B: Environmental, 248 (2019) 129-146.

[74] Z. Lin, Y. Lu, J. Huang, A hierarchical Ag_2O-nanoparticle/TiO_2-nanotube composite derived from natural cellulose substance with enhanced photocatalytic performance, Cellulose, 26 (2019) 6683-6700.

[75] E. Ferdosi, H. Bahiraei, D. Ghanbari, Investigation the photocatalytic activity of $CoFe_2O_4$/ZnO and $CoFe_2O_4$/ZnO/Ag nanocomposites for purification of dye pollutants, Separation and Purification Technology, 211 (2019) 35-39.

[76] P. Fageria, S. Gangopadhyay, S. Pande, Synthesis of ZnO/Au and ZnO/Ag nanoparticles and their photocatalytic application using UV and visible light, RSC Advances., 4 (2014) 24962-24972.

[77] L. Yang, F. Wang, C. Shu, P. Liu, W. Zhang, S. Hu, An in-situ synthesis of Ag/AgCl/TiO_2/hierarchical porous magnesian material and its photocatalytic performance, Scientific reports, 6 (2016) 21617.

[78] N. Lenin, A. Karthik, M. Sridharpanday, M. Selvam, S.R. Srither, S. Arunmetha, P. Paramasivam, V. Rajendran, Electrical and magnetic behavior of iron doped nickel titanate (Fe^{3+}/$NiTiO_3$) magnetic nanoparticles, Journal of Magnetism and Magnetic Materials, 397 (2016) 281-286.

[79] Z. Dai, F. Qin, H. Zhao, J. Ding, Y. Liu, R. Chen, Crystal Defect Engineering of Aurivillius Bi_2MoO_6 by Ce Doping for Increased Reactive Species Production in Photocatalysis, ACS Catalysis, 6 (2016) 3180-3192.

[80] P. Raizada, A. Sudhaik, P. Singh, P. Shandilya, V.K. Gupta, A. Hosseini-Bandegharaei, S. Agrawal, Ag_3PO_4 modified phosphorus and sulphur co-doped graphitic carbon nitride as a direct Z-scheme photocatalyst for 2, 4-dimethyl phenol degradation, Journal of Photochemistry and Photobiology A: Chemistry, 374 (2019) 22-35.

[81] C. Han, M. Pelaez, V. Likodimos, A.G. Kontos, P. Falaras, K. O'Shea, D.D. Dionysiou, Innovative visible light-activated sulfur doped TiO_2 films for water treatment, Applied Catalysis B: Environmental, 107 (2011) 77-87.

[82] X.-K. Wang, C. Wang, W.-L. Guo, J.-G. Wang, A novel single-step synthesis of N-doped TiO_2 via a sonochemical method, Materials Research Bulletin, 46 (2011) 2041-2044.

[83] M.V. Dozzi, L. Artiglia, G. Granozzi, B. Ohtani, E. Selli, Photocatalytic Activity vs Structural Features of Titanium Dioxide Materials Singly Doped or Codoped with Fluorine and Boron, The Journal of Physical Chemistry C, 118 (2014) 25579-25589.

[84] W.T. Li, W.Z. Huang, H. Zhou, H.Y. Yin, Y.F. Zheng, X.C. Song, Synthesis and photoactivity enhancement of Ba doped Bi_2WO_6 photocatalyst, Materials Research Bulletin, 64 (2015) 432-437.

[85] T.-T. Pham, S.G. Kang, E.W. Shin, Optical and structural properties of Mo-doped $NiTiO_3$ materials synthesized via modified Pechini methods, Applied Surface Science, 411 (2017) 18-26.

[86] I.N. Reddy, C.V. Reddy, J. Shim, B. Akkinepally, M. Cho, K. Yoo, D. Kim, Excellent visible-light driven photocatalyst of (Al, Ni) co-doped ZnO structures for organic dye degradation, Catalysis Today, (2018).

[87] D. Ramimoghadam, S. Bagheri, S.B.A. Hamid, Progress in electrochemical synthesis of magnetic iron oxide nanoparticles, Journal of Magnetism and Magnetic Materials, 368 (2014) 207-229.

[88] C.Y. Su, L.C. Wang, W.S. Liu, C.C. Wang, T.P. Perng, Photocatalysis and Hydrogen Evolution of Al- and Zn-Doped TiO_2 Nanotubes Fabricated by Atomic Layer Deposition, ACS applied materials & interfaces, 10 (2018) 33287-33295.

[89] S. Irfan, S. Rizwan, Y. Shen, L. Li, Asfandiyar, S. Butt, C.W. Nan, The Gadolinium ($Gd(^{3+})$) and Tin ($Sn(^{4+})$) Co-doped $BiFeO_3$ Nanoparticles as New Solar Light Active Photocatalyst, Scientific reports, 7 (2017) 42-49.

[90] I. Udom, Y. Zhang, M.K. Ram, E.K. Stefanakos, A.F. Hepp, R. Elzein, R. Schlaf, D.Y. Goswami, A simple photolytic reactor employing Ag-doped ZnO nanowires for water purification, Thin Solid Films, 564 (2014) 258-263.

[91] K. Kondo, N. Murakami, C. Ye, T. Tsubota, T. Ohno, Development of highly efficient sulfur-doped TiO_2 photocatalysts hybridized with graphitic carbon nitride, Applied Catalysis B: Environmental, 142-143 (2013) 362-367.

[92] Y. Niu, M. Xing, B. Tian, J. Zhang, Improving the visible light photocatalytic activity of nano-sized titanium dioxide via the synergistic effects between sulfur doping and sulfation, Applied Catalysis B: Environmental, 115-116 (2012) 253-260.

[93] Z. Wei, T. Xinyue, W. Xiaomeng, D. Benlin, Z. Lili, X. Jiming, F. Yue, S. Ni, Z. Fengxia, Novel p-n heterojunction photocatalyst fabricated by flower-like $BiVO_4$ and Ag_2S nanoparticles: Simple synthesis and excellent photocatalytic performance, Chemical Engineering Journal, 361 (2019) 1173-1181.

[94] N.S. Gultom, H. Abdullah, D.-H. Kuo, W.-C. Ke, Oriented p–n Heterojunction Ag_2O/Zn(O,S) Nanodiodes on Mesoporous SiO_2 for Photocatalytic Hydrogen Production, ACS Applied Energy Materials, 2 (2019) 3228-3236.

[95] C. Liu, F. Meng, L. Zhang, D. Zhang, S. Wei, K. Qi, J. Fan, H. Zhang, X. Cui, CuO/ZnO heterojunction nanoarrays for enhanced photoelectrochemical water oxidation, Applied Surface Science, 469 (2019) 276-282.

[96] J. Zhu, J. He, L. Hu, A novel Cu_2O@$HNbWO_6$ heterojunction photocatalyst with enhanced photocatalytic performance, Materials Letters, 254 (2019) 297-300.

[97] R. Ji, M. Zhang, W. Ma, Z. Zhu, C. Ma, P. Huo, Y. Yan, Y. liu, C. Li, Heterojunction photocatalyst fabricated by deposition Co_3O_4 nanoparticles on MoS_2 nanosheets with enhancing photocatalytic performance and mechanism insight, Journal of the Taiwan Institute of Chemical Engineers, 97 (2019) 158-169.

[98] R. Li, M. Cai, Z. Xie, Q. Zhang, Y. Zeng, H. Liu, G. Liu, W. Lv, Construction of heterostructured $CuFe_2O_4$/g-C_3N_4 nanocomposite as an efficient visible light photocatalyst with peroxydisulfate for the organic oxidation, Applied Catalysis B: Environmental, 244 (2019) 974-982.

[99] C. Lin, X. Xie, C. Li, Q. Yan, $Co_{0.5}Zn_{0.5}Fe_2O_4$/Ag_3PO_4 : A magnetic, highly efficient visible-light photocatalyst and the Z-scheme mechanism for removal of anionic dye and tetracycline hydrochloride, Materials Science in Semiconductor Processing, 82 (2018) 46-53.

[100] R. Abazari, A.R. Mahjoub, Potential Applications of Magnetic β-$AgVO_3$/$ZnFe_2O_4$ Nanocomposites in Dyes, Photocatalytic Degradation, and Catalytic Thermal Decomposition of Ammonium Perchlorate, Industrial & Engineering Chemistry Research, 56 (2017) 623-634.

[101] S. Ferrari, R.S. Kumar, F. Grinblat, J.C. Aphesteguy, F.D. Saccone, D. Errandonea, In-situ high-pressure x-ray diffraction study of zinc ferrite nanoparticles, Solid State Sciences, 56 (2016) 68-72.

[102] K. Kombaiah, J.J. Vijaya, L.J. Kennedy, M. Bououdina, Studies on the microwave assisted and conventional combustion synthesis of Hibiscus rosa-sinensis plant extract based $ZnFe_2O_4$

nanoparticles and their optical and magnetic properties, Ceramics International, 42 (2016) 2741-2749.

[103] C. Zhao, C. Shao, X. Li, X. Li, R. Tao, X. zhou, Y. Liu, Magnetically separable $Bi_2MoO_6/ZnFe_2O_4$ heterostructure nanofibers: Controllable synthesis and enhanced visible light photocatalytic activity, Journal of Alloys and Compounds, 747 (2018) 916-925.

[104] S.G. Khasevani, M.R. Gholami, Synthesis of BiOI/$ZnFe_2O_4$–Metal–Organic Framework and g-C_3N_4-Based Nanocomposites for Applications in Photocatalysis, Industrial & Engineering Chemistry Research, 58 (2019) 9806-9818.

[105] J. Li, Z. Liu, Z. Zhu, Magnetically separable $ZnFe_2O_4$, $Fe_2O_3/ZnFe_2O_4$ and $ZnO/ZnFe_2O_4$ hollow nanospheres with enhanced visible photocatalytic properties, RSC Advances, 4 (2014) 51302-51308.

[106] B. Safizade, S.M. Masoudpanah, M. Hasheminiasari, A. Ghasemi, Photocatalytic activity of $BiFeO_3/ZnFe_2O_4$ nanocomposites under visible light irradiation, RSC Advances, 8 (2018) 6988-6995.

[107] Z. Zhu, F. Liu, H. Zhang, J. Zhang, L. Han, Photocatalytic degradation of 4-chlorophenol over Ag/MFe_2O_4 (M = Co, Zn, Cu, and Ni) prepared by a modified chemical co-precipitation method: a comparative study, RSC Advances, 5 (2015) 55499-55512.

[108] C. Shifu, Z. Wei, L. Wei, Z. Huaye, Y. Xiaoling, C. Yinghao, Preparation, characterization and activity evaluation of p-n junction photocatalyst p-$CaFe_2O_4$/n-Ag_3VO_4 under visible light irradiation, Journal of hazardous materials, 172 (2009) 1415-1423.

[109] L. Jing, Y. Xu, C. Qin, J. Liu, S. Huang, M. He, H. Xu, H. Li, Visible-light-driven $ZnFe_2O_4/Ag/Ag_3VO_4$ photocatalysts with enhanced photocatalytic activity under visible light irradiation, Materials Research Bulletin, 95 (2017) 607-615.

[110] Z. Wei, F. Yue, Z. Jin, Z. Fengxia, S. Zhenhuan, D. Benlin, D.Y.C. Leung, Z. Lili, X. Jiming, Novel Ag/p-AgBr/n-$BiVO_4$ Plasmonic Heterojunction Photocatalyst: Study on the Excellent Photocatalytic Performance and Photocatalytic Mechanism, ACS Applied Energy Materials, 2 (2018) 694-704.

[111] W. Zhao, J. Zhang, F. Zhu, F. Mu, L. Zhang, B. Dai, J. Xu, A. Zhu, C. Sun, D.Y.C. Leung, Study the photocatalytic mechanism of the novel Ag/p-Ag_2O/n-$BiVO_4$ plasmonic photocatalyst for the simultaneous removal of BPA and chromium(VI), Chemical Engineering Journal, 361 (2019) 1352-1362.

[112] S. Iravani, Green synthesis of metal nanoparticles using plants, Green Chemistry, 13 (2011) 26-38.

[113] I. Kumar, M. Mondal, V. Meyappan, N. Sakthivel, Green one-pot synthesis of gold nanoparticles using Sansevieria roxburghiana leaf extract for the catalytic degradation of toxic organic pollutants, Materials Research Bulletin, 117 (2019) 18-27.

[114] M. Madhukara Naik, H.S. Bhojya Naik, G. Nagaraju, M. Vinuth, H. Raja Naika, K. Vinu, Green synthesis of zinc ferrite nanoparticles in Limonia acidissima juice: Characterization and their application as photocatalytic and antibacterial activities, Microchemical Journal, 146 (2019) 1227-1235.

[115] M. Sriramulu, D. Shukla, S. Sumathi, Aegle marmelos leaves extract mediated synthesis of zinc ferrite: Antibacterial activity and drug delivery, Materials Research Express, 5 (2018) 115-404.

[116] S. Lunge, S. Singh, A. Sinha, Magnetic iron oxide (Fe_3O_4) nanoparticles from tea waste for arsenic removal, Journal of Magnetism and Magnetic Materials, 356 (2014) 21-31.

[117] P. Laokul, V. Amornkitbamrung, S. Seraphin, S. Maensiri, Characterization and magnetic properties of nanocrystalline $CuFe_2O_4$, $NiFe_2O_4$, $ZnFe_2O_4$ powders prepared by the Aloe vera extract solution, Current Applied Physics, 11 (2011) 101-108.

[118] S.B. Patil, H.S. Bhojya Naik, G. Nagaraju, R. Viswanath, S.K. Rashmi, M. Vijay kumar, Sugarcane juice mediated eco-friendly synthesis of visible light active zinc ferrite nanoparticles: Application to degradation of mixed dyes and antibacterial activities, Materials Chemistry and Physics, 212 (2018) 351-362.

[119] N. Matinise, K. Kaviyarasu, N. Mongwaketsi, S. Khamlich, L. Kotsedi, N. Mayedwa, M. Maaza, Green synthesis of novel zinc iron oxide ($ZnFe_2O_4$) nanocomposite via Moringa Oleifera natural extract for electrochemical applications, Applied Surface Science, 446 (2018) 66-73.

[120] K. Kombaiah, J.J. Vijaya, L.J. Kennedy, M. Bououdina, H.A. Al-Lohedan, R.J. Ramalingam, Studies on Opuntia dilenii haw mediated multifunctional $ZnFe_2O_4$ nanoparticles: Optical, magnetic and catalytic applications, Materials Chemistry and Physics, 194 (2017) 153-164.

[121] R.S. Yadav, I. Kuřitka, J. Vilcakova, P. Urbánek, M. Machovsky, M. Masař, M. Holek, Structural, magnetic, optical, dielectric, electrical and modulus spectroscopic characteristics of $ZnFe_2O_4$ spinel ferrite nanoparticles synthesized via honey-mediated sol-gel combustion method, Journal of Physics and Chemistry of Solids, 110 (2017) 87-99.

[122] T.-y. Wang, Q. Li, K.-s. Bi, Bioactive flavonoids in medicinal plants: Structure, activity and biological fate, Asian Journal of Pharmaceutical Sciences, 13 (2018) 12-23.
[123] H. Yang, J. Tian, T. Li, H. Cui, Synthesis of novel Ag/Ag_2O heterostructures with solar full spectrum (UV, visible and near-infrared) light-driven photocatalytic activity and enhanced photoelectrochemical performance, Catalysis Communications, 87 (2016) 82-85.
[124] I. Bibi, N. Nazar, M. Iqbal, S. Kamal, H. Nawaz, S. Nouren, Y. Safa, K. Jilani, M. Sultan, S. Ata, F. Rehman, M. Abbas, Green and eco-friendly synthesis of cobalt-oxide nanoparticle: Characterization and photo-catalytic activity, Advanced Powder Technology, 28 (2017) 2035-2043.
[125] T.B. Tafesse, A. Hymete, Y. Mekonnen, M. Tadesse, Antidiabetic activity and phytochemical screening of extracts of the leaves of Ajuga remota Benth on alloxan-induced diabetic mice, BMC complementary and alternative medicine, 17 (2017) 243.
[126] S.N. Rishikeshi, S.S. Joshi, M.K. Temgire, J.R. Bellare, Chain length dependence of polyol synthesis of zinc ferrite nanoparticles: why is diethylene glycol so different?, Dalton Trans, 42 (2013) 5430-5438.
[127] R. Sai, S.D. Kulkarni, K.J. Vinoy, N. Bhat, S.A. Shivashankar, $ZnFe_2O_4$: Rapid and sub-100 °C synthesis and anneal-tuned magnetic properties, J. Mater. Chem., 22 (2012) 2149-2156.
[128] J. Ye, S.Q. Liu, W.X. Liu, Z.D. Meng, L. Luo, F. Chen, J. Zhou, Photocatalytic Simultaneous Removal of Nitrite and Ammonia via a Zinc Ferrite/Activated Carbon Hybrid Catalyst under UV-Visible Irradiation, ACS omega, 4 (2019) 6411-6420.
[129] W. Ding, L. Zhao, H. Yan, X. Wang, X. Liu, X. Zhang, X. Huang, R. Hang, Y. Wang, X. Yao, B. Tang, Bovine serum albumin assisted synthesis of $Ag/Ag_2O/ZnO$ photocatalyst with enhanced photocatalytic activity under visible light, Colloids and Surfaces A: Physicochemical and Engineering Aspects, 568 (2019) 131-140.
[130] H.Znao, X.Liu, Y.Dong, H.Wang, A novel visible light driven ternary $Ag@Ag_2O/BiOCl$ Z-scheme photocatalyst with enhanced removal efficiency of RhB, RSC Advances.
[131] A. Manikandan, J. Judith Vijaya, M. Sundararajan, C. Meganathan, L.J. Kennedy, M. Bououdina, Optical and magnetic properties of Mg-doped $ZnFe_2O_4$ nanoparticles prepared by rapid microwave combustion method, Superlattices and Microstructures, 64 (2013) 118-131.
[132] M. Mokhtar Mohamed, M. Khairy, A. Ibrahem, P-n junction based $Ag_2O@Ag@$Coated functionalized carbon nanotubes and their efficient visible-light photocatalytic reduction performances, Microporous and Mesoporous Materials, 292 (2020) 109734.

[133] A. Tadjarodi, M. Imani, M. Salehi, $ZnFe_2O_4$ nanoparticles and a clay encapsulated $ZnFe_2O_4$ nanocomposite: synthesis strategy, structural characteristics and the adsorption of dye pollutants in water, RSC Advances, 5 (2015) 56145-56156.
[134] D. Neravathu, A.R. Paloly, S. P, S. M, M.J. Bushiri, Hybrid nanomaterial of $ZnFe_2O_4$/α-Fe_2O_3 implanted graphene for electrochemical glucose sensing application, Diamond and Related Materials, 106 (2020) 107852.
[135] M. Madhukara Naik, H.S. Bhojya Naik, G. Nagaraju, M. Vinuth, K. Vinu, R. Viswanath, Green synthesis of zinc doped cobalt ferrite nanoparticles: Structural, optical, photocatalytic and antibacterial studies, Nano-Structures & Nano-Objects, 19 (2019) 100322.
[136] J. Ma, C. Liu, K. Chen, Counting on low-oxygen calcination to boost zinc ferrite powder's topology and photocatalytic efficiency, Advanced Powder Technology, 31 (2020) 1372-1380.
[137] M.L. Baynosa, A.H.Mady, V.Q. Ngaya D.R. Kumar, M.S. sayed, D.Tuma, J.J.Shim, Ecofriendly synthesis of recyclable mesoporous Zinc ferrite @ reduced graphene oxide nanocomposite for eficient photocatalytic dye degradation under solar radiation, (2019) 1-11.
[138] H. Xu, J. Xie, W. Jia, G. Wu, Y. Cao, The formation of visible light-driven Ag/Ag_2O photocatalyst with excellent property of photocatalytic activity and photocorrosion inhibition, Journal of colloid and interface science, 516 (2018) 511-521.